

JGR Solid Earth

RESEARCH ARTICLE

10.1029/2024JB030601

Key Points:

- We pursue community efforts to develop code verification benchmarks for 2-D quasi-dynamic fluid-induced faulting problems
- We obtain quantitative agreements among simulations of fluid-induced aseismic slip transients for different numerical methods
- The spatio-temporal evolution of aseismic fault slip can depend on treatments of fault friction given the same pore pressure evolution

Supporting Information:

Supporting Information may be found in the online version of this article.

Correspondence to:

V. R. Lambert,
valerelambert@protonmail.ch

Citation:

Lambert, V. R., Erickson, B. A., Jiang, J., Dunham, E. M., Kim, T., Ampuero, J.-P., et al. (2025). Community-driven code comparisons for simulations of fluid-induced aseismic slip. *Journal of Geophysical Research: Solid Earth*, 130, e2024JB030601. <https://doi.org/10.1029/2024JB030601>

Received 23 OCT 2024

Accepted 18 MAR 2025

Author Contributions:

Conceptualization: Valère R. Lambert, Brittany A. Erickson, Junle Jiang, Eric M. Dunham

Data curation: Valère R. Lambert, Brittany A. Erickson, Taeho Kim, Pierre Dublanchet, Meng Li, Jasper Marcum, Md Shumon Mia, So Ozawa, Pierre Romanet, Yuyun Yang, Jeena Yun

Formal analysis: Valère R. Lambert

Funding acquisition: Valère R. Lambert, Brittany A. Erickson, Junle Jiang, Eric M. Dunham, Jean-Paul Ampuero, Ryosuke Ando, Frédéric Cappa

© 2025. The Author(s).

This is an open access article under the terms of the Creative Commons Attribution-NonCommercial-NoDerivs License, which permits use and distribution in any medium, provided the original work is properly cited, the use is non-commercial and no modifications or adaptations are made.

Community-Driven Code Comparisons for Simulations of Fluid-Induced Aseismic Slip



Valère R. Lambert¹ , Brittany A. Erickson², Junle Jiang³ , Eric M. Dunham⁴ , Taeho Kim⁵ , Jean-Paul Ampuero⁶ , Ryosuke Ando⁷ , Frédéric Cappa⁶ , Pierre Dublanchet⁸ , Ahmed Elbanna⁹, Yuri Fialko¹⁰ , Alice-Agnes Gabriel^{10,11} , Nadia Lapusta⁵ , Meng Li¹² , Jasper Marcum² , David May¹⁰ , Md Shumon Mia^{9,13} , So Ozawa⁴ , Casper Pranger¹¹ , Pierre Romanet^{6,14} , Marco M. Scuderi¹⁴ , Ylona van Dinther¹², Yuyun Yang^{15,16} , and Jeena Yun¹⁰ 

¹Department of Earth and Planetary Sciences, University of California, Santa Cruz, CA, USA, ²Department of Computer and Information Science, University of Oregon, Eugene, OR, USA, ³School of Geosciences, University of Oklahoma, Norman, OK, USA, ⁴Department of Geophysics, Stanford University, Stanford, CA, USA, ⁵Seismological Laboratory and Department of Mechanical and Civil Engineering, California Institute of Technology, Pasadena, CA, USA, ⁶Université Côte d'Azur, CNRS, Observatoire de la Côte d'Azur, IRD, Sophia-Antopolis, France, ⁷University of Tokyo, Bunkyo City, Japan, ⁸Mines Paris, Paris Sciences & Lettres University, Paris, France, ⁹Department of Civil and Environmental Engineering, University of Illinois Urbana-Champaign, Urbana-Champaign, IL, USA, ¹⁰Scripps Institution of Oceanography, University of California, San Diego, CA, USA, ¹¹Department of Earth and Environmental Sciences, Ludwig-Maximilians-Universität München, Munich, Germany, ¹²Department of Earth Sciences, Utrecht University, Utrecht, The Netherlands, ¹³Bangladesh University of Engineering and Technology, Dhaka, Bangladesh, ¹⁴Department of Earth Sciences, La Sapienza University of Rome, Rome, Italy, ¹⁵Division of Industrial Data Science, School of Data Science, Lingnan University, Tuen Mun, Hong Kong, ¹⁶The Chinese University of Hong Kong, Ma Liu Shui, Hong Kong

Abstract Numerical simulations of Sequences of Earthquakes and Aseismic Slip (SEAS) have rapidly progressed to address fundamental problems in fault mechanics and provide self-consistent, physics-based frameworks to interpret and predict geophysical observations across spatial and temporal scales. To advance SEAS simulations with rigor and reproducibility, we pursue community efforts to verify numerical codes in an expanding suite of benchmarks. Here we present code comparison results from a new set of quasi-dynamic benchmark problems BP6-QD-A/S/C that consider an aseismic slip transient induced by changes in pore fluid pressure consistent with fluid injection and diffusion in fault models with different treatments of fault friction. Ten modeling groups participated in problems BP6-QD-A and BP6-QD-S considering rate-and-state fault models using the aging (-A) and slip (-S) law formulations for frictional state evolution, respectively, allowing us to better understand how various computational factors across codes affect the simulated evolution of pore pressure and aseismic slip. Comparisons of problems using the aging versus slip law, and a constant friction coefficient (-C), illustrate how aseismic slip models can differ in the timing and amount of slip achieved with different treatments of fault friction given the same perturbations in pore fluid pressure. We achieve excellent quantitative agreement across participating codes, with further agreement attained by ensuring sufficiently fine time-stepping and consistent treatment of boundary conditions. Our benchmark efforts offer a community-based example to reveal sensitivities of numerical modeling results, which is essential for advancing multi-physics SEAS models to better understand and construct reliable predictive models of fault dynamics.

Plain Language Summary Fault motion is accommodated through an array of seismic (earthquake-producing) and aseismic (slow) deformation processes spanning time scales ranging from milliseconds to millennia and longer. Computational models are used to simulate Sequences of Earthquakes and Aseismic Slip (SEAS) in order to bridge insight between different geophysical observations and shed light on underlying physical conditions governing fault dynamics. An area of growing interest is the development of modeling frameworks aimed at exploring how subsurface fluids in the Earth influence fault slip, which is highly relevant to understanding natural seismicity patterns as well as induced seismicity resulting from human activities, such as energy resource practices. To improve these simulations, we pursue community efforts to design benchmarks for SEAS problems and involve researchers around the globe to compare simulation results using different numerical codes. We use the ensemble of simulation results from different codes to examine the sensitivity of simulated fluid flow and fault slip to different computational factors. These exercises are important for

Pierre Dublanchet, Ahmed Elbanna,
Yuri Fialko, Alice-Agnes Gabriel,
Nadia Lapusta, So Ozawa,
Pierre Romanet, Marco M. Scuderi,
Ylona van Dinther, Yuyun Yang

Investigation: Valère R. Lambert,
Brittany A. Erickson, Junle Jiang, Eric
M. Dunham, Taeho Kim,
Pierre Dublanchet, Ahmed Elbanna, Alice-
Agnes Gabriel, Nadia Lapusta, Meng Li,
Jasper Marcum, David May, Md
Shumon Mia, So Ozawa, Casper Pranger,
Pierre Romanet, Ylona van Dinther,
Yuyun Yang, Jeena Yun

Methodology: Valère R. Lambert,
Brittany A. Erickson, Junle Jiang, Eric
M. Dunham

Project administration: Valère
R. Lambert, Brittany A. Erickson,
Junle Jiang

Writing – original draft: Valère
R. Lambert

Writing – review & editing: Valère
R. Lambert, Brittany A. Erickson,
Junle Jiang, Eric M. Dunham, Taeho Kim,
Ryosuke Ando, Pierre Dublanchet,
Ahmed Elbanna, Yuri Fialko, Alice-
Agnes Gabriel, Nadia Lapusta, Meng Li,
Jasper Marcum, David May, Md
Shumon Mia, So Ozawa, Casper Pranger,
Pierre Romanet, Ylona van Dinther,
Yuyun Yang, Jeena Yun

promoting a new generation of advanced models capable of resolving multiple physical processes governing faulting dynamics. Understanding the sensitivity of simulation outputs will help test models against real-world observations and the reliability of physics-based predictive models.

1. Introduction

Fault motion can be accommodated through sequences of seismic (earthquake-producing) events as well as complex patterns of aseismic (slow) slip. An array of physics-based computational modeling frameworks exist to explore these problems, bridge observations from the lab and field across spatial and temporal scales, and develop predictive models of seismic hazards. On one end of the modeling spectrum, single dynamic rupture simulations serve as powerful tools to study the influence of fault structure, constitutive behaviors, wave propagation, and prestress on the dynamics of earthquake rupture and associated ground motion (e.g., Bhat et al., 2007; Day, 1982; Dunham et al., 2011a; Dunham et al., 2011b; Gabriel et al., 2012; J. E. Kozdon & Dunham, 2013; Lozos et al., 2011; Ma & Elbanna, 2019; Nielsen et al., 2000; Olsen et al., 1997; Ripperger et al., 2007; Shi & Day, 2013; Ulrich et al., 2019; Xu et al., 2015). However, single-rupture simulations need to select initial conditions and impose nucleation procedures, requiring additional assumptions to incorporate the effects from the prior history of seismic and aseismic slip. On the other end of the modeling spectrum, several earthquake simulators have been developed to examine complex spatiotemporal characteristics of seismicity and simulate thousands to millions of earthquake ruptures across larger-scale fault networks (Richards-Dinger & Dieterich, 2012; Shaw et al., 2018; Tullis et al., 2012). Simulating such extensive earthquake catalogs over large fault networks requires the adoption of considerable simplifications and approximations for key physical features that may influence or dominate earthquake and faulting behaviors, such as wave-mediated stress changes, aseismic deformation, inelastic responses, as well as fluid effects.

It has become increasingly accepted that understanding the conditions governing fault motion, including how earthquakes start, grow, and stop, requires a better understanding of how the history of prior slip events, including past earthquakes and aseismic slip, modify stress and other initial conditions along faults prior to earthquake rupture. Numerical simulations of Sequences of Earthquakes and Aseismic Slip (SEAS) are well-suited to explore the physical conditions governing these problems, as they aim to resolve all styles of the deformation history on faults, from the spontaneous nucleation of transient slow slip and earthquakes, to rapid sub-second variations in motion during dynamic rupture, to periods of post-seismic slip relaxation and potentially millennia of slow loading. Such simulations also provide a unified, self-consistent framework for determining physical properties compatible with a range of observations including surface deformation, microseismicity, paleoseismic events, and thermal constraints, and hence may shed light on the current state of a fault segment or system and potential future rupture scenarios (e.g., Allison & Dunham, 2018; Barbot et al., 2012; Ben-Zion & Rice, 1997; Cattania, 2019; Chen & Lapusta, 2009; Erickson & Dunham, 2014; Jiang & Lapusta, 2016; Kaneko et al., 2010; Lambert & Barbot, 2016; Lambert, Lapusta, & Perry, 2021; Lapusta & Rice, 2003; Lapusta et al., 2000; Liu & Rice, 2005; Noda & Lapusta, 2013; Segall et al., 2010). With the aim of rigorously simulating deformation processes throughout the entire seismic cycle, SEAS modeling also provide a framework to determine physically justified approximations and self-consistent choices of initial conditions and earthquake nucleation procedures for detailed dynamic rupture simulations and earthquake simulators.

In addition to examining how earthquakes develop within the context of earthquake sequences, a unique component of SEAS modeling is the aim to capture how aseismic slip accommodates and redistributes stresses from tectonic motion, earthquakes, as well as perturbations from environmental or anthropogenic forcing, such as the subsurface injection of fluids from energy resource and waste management practices (e.g., Eyre et al., 2019; Guglielmi et al., 2015; Wei et al., 2015). Aseismic deformation processes have their own scientifically intriguing and societally relevant implications for fault mechanics and surface deformation (e.g., Hubbard & Mallick, 2021; Luo & Wang, 2022; Muto et al., 2019), as well as important implications for models of seismic hazard seeing that aseismic processes can influence the effective loading and fault conditions that govern the nucleation and growth of earthquakes (e.g., Barbot et al., 2012). Moreover, the discovery of episodic slow-slip events has motivated a plethora of studies on aseismic slip transients, their connection to fault physical conditions, and their relationship to earthquake nucleation, with potential implications for early warning and forecasting strategies (e.g., Ito et al., 2013; N. Kato, 2023; A. Kato et al., 2012; Liu, 2014; Liu & Rice, 2005, 2007; Michel et al., 2019; S. Ozawa

et al., 2002; S. W. Ozawa et al., 2019; Rogers & Dragert, 2003; Ruiz et al., 2014; Schwartz & Rokosky, 2007; Segall & Rice, 1995; Segall & Bradley, 2012; Segall et al., 2010; Romanet et al., 2018).

Developments in SEAS models over recent decades have explored increasingly diverse physical ingredients relevant to long-term slip such as interseismic healing of the fault zone, bulk elastic heterogeneity and plasticity, viscoelasticity, dynamic fault weakening, and fluid flow (e.g., Allison & Dunham, 2018; Barbot, 2018; Erickson & Dunham, 2014; Jiang & Lapusta, 2016; Lambert & Barbot, 2016; Mia et al., 2022; Noda et al., 2013; Thakur et al., 2020; Zhu et al., 2020). Of particular note is the investigation of different formulations and treatments of fault shear resistance and its evolution, and the role of fluid effects on faulting processes. Laboratory-derived rate-and-state friction laws (e.g., Dieterich, 2007) are fundamental ingredients in most SEAS models, providing an empirical unified description of how fault friction evolves with slip as well as the time-dependent healing or restrengthening of frictional resistance under negligible motion, which facilitates the reloading of faults in between accelerated slip events. Laboratory and theoretical studies continue to explore appropriate descriptions for fault shear resistance and its evolution with slip, time, confinement, temperature, and a number of other potential state variables, as well as implications for faulting phenomenon (e.g., Acosta et al., 2018; Barbot, 2022; Noël et al., 2023; Pignalberi et al., 2024; Shimamoto & Noda, 2014). For example, there is still much debate over the proper formulation for the evolution of the frictional state variable of rate-and-state friction laws, which aims to describe the evolution of frictional contact quality and/or quantity during sliding along with time-dependent healing. The two most commonly considered formulations for frictional state evolution are the aging and slip laws (Ruina, 1983), which characterize results from different sets of friction experiments. Velocity-stepping experiments demonstrating symmetric friction changes to velocity increases and decreases have favored the use of the slip law formulation for the state variable evolution (e.g., Bhattacharya et al., 2015; Blanpied et al., 1998). However, many SEAS models implement the aging law formulation, in part because the aging law captures the time-dependent healing observed in slide-hold-slide experiments (e.g., Beeler et al., 1994; Dieterich, 1979; Ruina, 1983), but also as frictional evolution using the slip law can be more computationally challenging to resolve given the more rapid evolution of the state variable with increasing slip (e.g., Ampuero & Rubin, 2008b).

The role of fluids in fault slip dynamics has also become an important topic of active research in fault mechanics, relevant to a variety of problems in the context of induced seismicity during energy production and wastewater disposal operations (e.g., Ellsworth, 2013; Lee et al., 2019; McGarr et al., 2015), as well as naturally occurring slip events and earthquake swarms, such as in Southern California (e.g., Hauksson et al., 2016; Khoshmanesh & Shirzaei, 2018; Ross et al., 2020; Wei et al., 2015), and subduction zone processes (e.g., Burgmann, 2018; Frank et al., 2015; Shelly et al., 2007). A number of studies have applied SEAS simulation techniques to study the role of fluids in faulting problems, including fluid injection and diffusion (Bhattacharya & Viesca, 2019; Dublanchet, 2019; Larochelle et al., 2021; Yang & Dunham, 2021, 2023; Zhu et al., 2020), as well as implications of (thermo-)hydro-mechanical processes for the nucleation and propagation of dynamic earthquake ruptures, such as fault gouge dilatancy, compaction, and the thermal pressurization of pore fluids (Lambert, Lapusta, & Faulkner, 2021; Noda et al., 2009; Noda & Lapusta, 2013; Segall & Bradley, 2012; Segall et al., 2010; Segall & Rice, 1995, 2006; Yang & Dunham, 2023). Such modeling frameworks can help determine and quantify which physical factors control the interplay between fluid flow and fault slip, their implications for diverse observables such as ground deformation and the frequency and size of seismicity, and assist in integrating laboratory and field observations to develop predictive models to inform faulting hazards as well as practices such as wastewater management from energy resource production.

With the continued development of increasingly sophisticated SEAS models aimed at explaining, reproducing, and predicting real-world faulting behaviors, efforts to verify numerical codes are essential to ensure that these methodologies produce accurate and reproducible results. This study constitutes ongoing community efforts in the SEAS working group, supported by the Statewide California Earthquake Center (SCEC), to develop an expanding suite of benchmark problems and perform code verification exercises for SEAS models. Inspired by the successes of the SCEC/USGS Spontaneous Rupture Code Verification Project (Barall & Harris, 2014; Harris et al., 2009, 2018), the SEAS initiative has set out to facilitate community code comparisons, and verify and advance the next generation of physics-based earthquake and faulting models that resolve all phases of the earthquake cycle and slow-slip phenomena. Through our prior community exercises, we have achieved excellent agreement between simulations from a growing cohort of modeling groups for a range of problems considering earthquake sequences on 2-D and 3-D fault models obeying rate-and-state friction with different treatments of

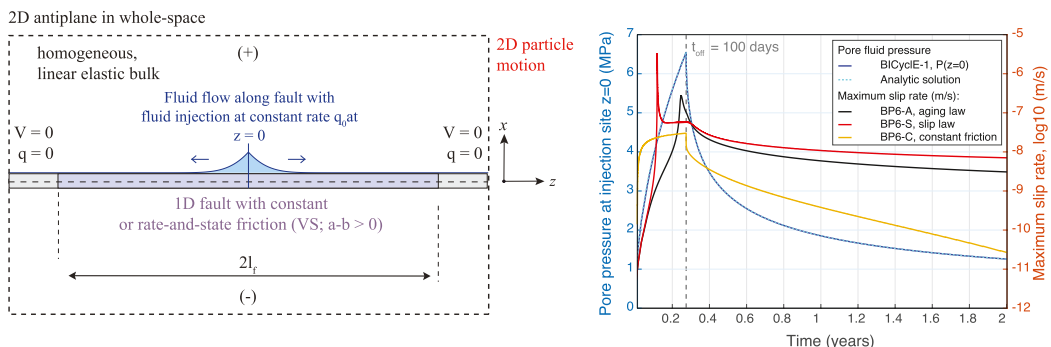


Figure 1. Benchmark problem BP6-QD considers a 2-D antiplane problem for a planar fault embedded in a homogeneous whole-space that responds in a linear elastic manner to slip (Left). Fault slip is induced within a frictional region ($|z| \leq l_f$, blue) by pore pressure perturbations due to the injection of fluid in the middle of the fault ($z = 0$) and the along-fault diffusion of pore fluids. Fluid injection persists at a constant rate until a time $t_{\text{off}} = 100$ days, after which injection is shut off (Right). The fault response is examined in problem formulations considering rate-and-state fault models governed by the aging (BP6-A, red) or slip (BP6-S, black) law formulations of the frictional state variable evolution, or constant friction (BP6-C, orange). Simulations results are shown for spectral boundary element method (SBEM) code BICyclE-1, with simulated pore pressure evolution (dark blue) at the injection site ($z = 0$) being virtually identical to the corresponding analytic solution (dashed light blue, Supporting Information S1; Carslaw & Jaeger, 1959).

inertial (wave-mediated) effects and dipping fault geometries under slow tectonic loading (Erickson et al., 2020, 2023; Jiang et al., 2022). These comparisons have allowed us to assess relative sensitivities of simulated short- and long-term fault processes as well as different observables, including recurrence intervals, surface displacements, and statistics of simulated earthquakes, to numerical factors, such as treatments of the computational domain, boundary conditions, and numerical resolution.

Motivated by the goal of better understanding the sensitivity of simulated aseismic slip transients in SEAS models with multiple coupled physical processes, here we introduce a suite of 2-D quasi-dynamic (QD) benchmark exercises BP6-QD-A/S/C that focus on simulating a single fluid-induced aseismic slip event resulting from direct in-fault fluid injection and along-fault diffusion. While our previous SEAS benchmarks have examined earthquake occurrence in response to changes in shear stress consistent with long-term tectonic-like loading (e.g., from deep creep beneath the seismogenic zone, Erickson et al., 2020; Jiang et al., 2022; Erickson et al., 2023), our new suite of benchmarks focus on fault slip that is induced by pore fluid pressure changes as well as differences in the initiation and propagation of aseismic slip due to different treatments of fault friction evolution with slip (Figure 1). We present descriptions of our newly developed benchmark problems, BP6-QD, as well as community-driven code comparison results for problem formulations considering rate-and-state fault models using the aging (BP6-QD-A) versus slip (BP6-QD-S) law formulations of the frictional state variable. We introduce new quantitative metrics designed to facilitate comparison of simulation results across participating codes and to examine the sensitivity of the simulated pore fluid pressure and aseismic slip evolution to different computational factors. Through these efforts, we aim to promote a new generation of rigorous and robust numerical codes for solving multi-physics SEAS problems.

2. Benchmark Strategy and SEAS Coordination

The principle objective of the SEAS working group is to verify SEAS models that address important problems in earthquake science and fault mechanics. Our efforts have examined the dependence of simulated fault slip history on a number of physical and numerical modeling factors, such as initial conditions, fault properties, model spin-up, computational domain size and boundary conditions, as well as fault dip angle and treatments of inertial (wave-mediated) effects during dynamic rupture (Erickson et al., 2020, 2023; Jiang et al., 2022). An important balance in our benchmark design is the progressive exploration of new physical ingredients in SEAS models while maintaining reasonable benchmark complexity to maximize participation within the scientific community. As a guiding principle, we aim to start simple and incrementally add complexity over a series of SEAS benchmarks.

Table 1

BP6-QD: Details of Participating Sequences of Earthquakes and Aseismic Slip Codes and Modeling Groups

Code name	Type	Simulation [†] (Group Members)	References
BICycle-1	SBEM	kim (Kim, Lapusta)	(Lapusta et al., 2000; Lapusta & Liu, 2009)
BICycle-2		lambert (Lambert)	
QDBIM	BEM	lambert.2 (Lambert)	https://github.com/vlambert/QDBIM
Thrare	FDM	marcum (Marcum, Erickson)	(J. Kozdon et al., 2020; Erickson et al., 2022) https://github.com/Thrare/Thrare.jl
HBI	BEM	ozawa (Ozawa, Ando, Dunham)	(S. Ozawa et al., 2024) https://github.com/sozawa94/hbi
Scycle	FDM	yang (Yang, Dunham)	(Yang & Dunham, 2021; Zhu et al., 2020)
FastCycles	SBEM	romanet (Romanet)	(Romanet & Ozawa, 2021)
FEBE	Hybrid FEM/SBEM	msmia (Mia, Elbanna)	(Abdelmeguid et al., 2019; Hajarolasvadi & Elbanna, 2017)
GARNET	FDM	li (M. Li, Pranger, van Dinther)	(Li et al., 2022; Pranger, 2020) https://bitbucket.org/cpranger/garnet/
Tandem	DGFEM	yun (Yun, Gabriel, May, Fialko)	(Uphoff et al., 2022) https://github.com/TEAR-ERC/tandem
Dublanchet (2019)	SBEM	dublanchet (Dublanchet)	(Dublanchet, 2019)

[†] The names of simulations displayed on our online platform. FDM, Finite difference method; FEM, finite-element method; SBEM, spectral boundary element method; BEM, boundary element method; and DGFEM, discontinuous-Galerkin finite-element method.

BP6-QD focuses on examining the ability of different computational methods to accurately resolve aseismic slip processes. We begin with the relatively simple scenario considering the initiation and propagation of a single aseismic slip transient. At the same time, benchmark problems BP6-QD-A/S/C explore the incorporation of two new physical ingredients in our SEAS benchmark exercises. BP6-QD is our first set of benchmarks considering the effects of pore fluids in faulting problems, with the aseismic slip transient being induced by changes in pore fluid pressure consistent with the injection of fluids directly into the fault as well as along-fault fluid diffusion. As a starting point, we consider the one-way coupling of changes in pore fluid pressure, and hence effective normal stress, on fault slip. In other words, changes in pore fluid pressure influence fault slip behavior, however the mechanical deformation due to fault slip is assumed to not influence the fluid transport properties or pore fluid pressure evolution in benchmark problem BP6-QD.

In addition, benchmark problems BP6-QD-A/S/C consist of three problem formulations considering the propagation of a fluid-induced aseismic slip transient in models using different treatments of fault friction. Two versions consider a fault governed by rate-and-state friction using the aging (BP6-QD-A) and slip (BP6-QD-S) law formulations for the frictional state evolution with time and slip. This constitutes our first benchmark problem (BP6-QD-S) using the slip law formulation for state variable evolution in rate-and-state friction, whereas prior benchmark problems all considered the aging law formulation, as done in problem BP6-QD-A. The third version, BP6-QD-C, considers a fault with a constant friction coefficient.

A total of 10 modeling groups with 10 different simulation codes participated in both problems BP6-QD-A and BP6-QD-S. Our benchmark exercises provide a well-defined mathematical problem description, however modeling groups must formulate the problem and determine appropriate model parameters depending on their particular numerical framework. For example, the benchmark problem considers an infinite spatial domain, however some numerical schemes consider a finite domain and must thus determine choices for the model domain size and boundary conditions that effectively represent the infinite space, as discussed further in Section 3.3. Details of the codes and modeling groups are provided in Tables 1 and 2, along with a summary of computational methods, including spectral boundary element/boundary element (spectral boundary element method, SBEM/boundary element method, BEM), finite difference (FDM), and discontinuous-Galerkin/finite element (DGFEM/finite-element method, FEM) methods, as well as specific choices for important parameters.

In order to simulate fault motion over a wide range of time scales, SEAS models typically employ adaptive time-stepping methods that vary the size of the computational time step based on the need to resolve physical processes occurring at different rates. A goal of benchmark problem BP6-QD is to examine the sensitivity of simulated aseismic slip to employed modeling approaches, such as time-stepping methods, specifically here in the context of multi-physics frictional faulting problems with the need to resolve both the evolution of pore fluid pressure and

Table 2

Computational Parameters and Methods Used in Codes for BP6-QD

Code name	L_x, L_z	Δz (on-fault)	Remote BC	Time stepping	Pore pressure evolution
BICycle-1	(∞ , 50 km)	10 m	periodic along-z, zero disp. at $x \rightarrow \infty$	(Lapusta et al., 2000)	implicit (BE)
BICycle-2	(∞ , 42 km)	10 m	periodic along-z, zero disp. at $x \rightarrow \infty$	(Lapusta et al., 2000), $\Delta t_{\max} = 500$ s	explicit (FE)
QDBIM	(∞ , 40 km)	10 m	zero disp.	RKDP45	explicit (FE)
Thrash	(40 km, 40 km)	25 m	zero disp.	RKDP45	analytic
HBI	(∞ , 40 km)	10 m	zero disp.	RKCK45	implicit (BE)
Scycle	(160 km, 160 km)	10 m	zero disp.	RK43, $\Delta t_{\max} = 1000$ s	implicit (BE)
FastCycles	(∞ , 163.84 km)	10 m	periodic along-z, zero disp. at $x \rightarrow \infty$	(Romanet & Ozawa, 2021)	analytic
FEBE	(∞ , 40 km)	10 m	periodic along-z, zero disp. at $x \rightarrow \infty$	(Lapusta et al., 2000)	analytic
GARNET	(50 km, 50 km)	10 m	traction-free	(Lapusta et al., 2000) with and w/out $\Delta t_{\max} = 500$ s	implicit (BE)
Tandem	(400 km, 400 km)	BP6-A 100 m BP6-S 50 m	zero disp.	RKDP45	analytic
Dublanchet (2019)	(∞ , 80 km)	9.77 m	zero disp.	RKF45	explicit (FE)

Note. L_x and L_z refer to model domain dimensions in the x and z directions, respectively. $L_x = \infty$ Refers to boundary element method/spectral boundary element method that consider the bulk response of a medium extending infinitely in the x -direction. Δz Refers to the on-fault spatial discretization where some codes use grid-stretching with larger computational cells further from the fault. Remote BC refers to the boundary conditions (BC) applied at the remote edges of the model domain. Runge-Kutta 4/5 time-stepping approaches are denoted by the use of Dormand-Prince (RKDP45), Fehlberg (RKF45), and Cash-Karp (RKCK45) methods. Numerical solutions for pore pressure evolution given by implicit backward Euler (BE) or explicit forward Euler (FE) integration.

fault slip. All groups that have submitted results for BP6-QD-A and BP6-QD-S apply either the adaptive time-stepping method of Lapusta et al. (2000) or some variant of a Runge-Kutta (RK)-like method. In order to ensure that the evolution of pore fluid pressure is sufficiently resolved, some groups have employed additional time step considerations to their chosen adaptive time-stepping methodology. Specific details can be found in Table 2 and are discussed later in the text as well as the references in Table 1. Note that each adaptive time-stepping method can be tuned through a number of internal parameters specific to the methodology, and we left this to participating groups to individually explore appropriate values.

In our benchmark exercises, we compare model outcomes across codes through visual inspection and quantitative assessment using metrics defined in Section 3.5. We first discuss comparisons for the original simulation results submitted by participating modeling groups, and include an additional suite of simulations performed to examine the sensitivity of results to modeling choices such as computational domain size and time-stepping procedures.

3. Benchmark Problem BP6-QD Description

Here we include specific details of the mathematical problem statement for BP6-QD-A/S/C, including coordinate system, boundary conditions, fault friction, and changes in pore fluid pressure (along with a description of relevant parameters) to aid in the analysis and discussion of results.

For the suite of benchmark problems BP6-QD-A/S/C, we assume that a planar fault is embedded in a homogeneous, isotropic, linear elastic whole-space defined by:

$$(x, y, z) \in (-\infty, \infty) \times (-\infty, \infty) \times (-\infty, \infty),$$

with the fault interface at $x = 0$, see Figure 1. We assume antiplane shear with the problem being reduced to two dimensions ($x - z$) and the only non-zero displacement being $u(x, z)$ in the out-of-plane y -direction.

We solve for the evolution of fault slip and shear stress within the fault region $z \in \Omega_f = (-l_f, l_f)$ that is consistent with the elastic material response and the fault friction law. The fault shear resistance F is assumed to be frictional:

$$F = (\bar{\sigma}_0 - p)f, \quad (1)$$

where f is the friction coefficient. $\bar{\sigma}_0 = \sigma - p_o$ represents the background effective normal stress, reflecting the difference between the total normal stress σ and the background pore pressure p_o , both assumed spatially uniform and fixed in time. Thus, changes in the effective normal stress:

$$\bar{\sigma}(z, t) = \bar{\sigma}_0 - p(z, t), \quad (2)$$

Arise from changes in pore fluid pressure $p(z, t)$ with respect to the background effective normal stress.

For the QD problems BP6-QD, motion and stress are governed by the equilibrium equation and Hooke's law for linear elasticity. The fault shear stress $\tau^0 + \Delta\tau(z, t) - \frac{\mu}{2c_s}V$ is the sum of the shear prestress, the shear stress change due to quasi-static elastic deformation, and the stress change from the radiation damping approximation (with prefactor $\mu/2c_s$ for antiplane shear given shear modulus μ , shear wave speed c_s , and slip rate V) to inertia. We impose no-slip ($V = 0$) conditions outside of the frictional domain Ω_f (i.e., $|z| > l_f$) and displacements u vanish at infinity, with no rigid body translation (i.e., no time-dependent loading). Note that for the 2-D problem, the antiplane shear and plane strain solutions for the quasi-static elastic response to slip on a planar fault in a uniform whole-space are identical with suitable interpretation of the elastic shear modulus μ in the antiplane shear case as $\mu/(1 - \nu)$ in the plane strain case, where ν is Poisson's ratio (Freund, 1998).

3.1. Fault Friction

3.1.1. Description of BP6-QD-A/S: Rate-And-State Friction

Problems BP6-QD-A and BP6-QD-S consider a fault governed by rate-and-state friction (Dieterich, 1979; Marone, 1998; Ruina, 1983), for which we equate the fault shear stress to the fault shear resistance F , which depends on slip rate V , state variable θ , and change in pore pressure p :

$$\tau = F(V, \theta, p). \quad (3)$$

The friction coefficient f is given by a regularized formulation (Lapusta et al., 2000):

$$f(V, \theta) = a \sinh^{-1} \left[\frac{V}{2V_*} \exp \left(\frac{f_* + b \ln(V_* \theta / D_{RS})}{a} \right) \right], \quad (4)$$

with the reference friction coefficient f_* at a reference slip rate V_* , and rate-and-state direct effect and evolution parameters a and b , respectively. BP6-QD-A/S both consider a fault governed by uniform velocity-strengthening (VS) friction, which inhibits spontaneous nucleation of frictional instability.

For BP6-QD-A, θ evolves according to the aging law (Dieterich, 1979; Ruina, 1983):

$$\frac{d\theta}{dt} = 1 - \frac{|V|\theta}{D_{RS}}, \quad (5)$$

where D_{RS} is the characteristic slip distance. For BP6-QD-S, θ evolves according to the slip law:

$$\frac{d\theta}{dt} = -\frac{|V|\theta}{D_{RS}} \ln \left[\frac{|V|\theta}{D_{RS}} \right]. \quad (6)$$

BP6-QD-S is our first benchmark problem to consider the slip law formulation (Equation 6) for the frictional state evolution, while prior benchmarks have used the aging law (Equation 5).

Table 3

Parameter Values Used in Benchmark Problems BP6-QD-A/S/C

Parameter	Definition	Value, units
μ	Shear modulus	32.04 GPa
ρ	Density	2,670 kg/m ³
c_s	Shear wave speed	3,464 km/s
σ_0	Initial effective normal stress	50 MPa
τ_{init}	Initial shear stress	29.2 MPa
q_0	Fluid injection rate	1.25×10^{-6} m/s
β	Pore and fluid compressibility	10^{-8} Pa ⁻¹
ϕ	Porosity	0.1
k	Permeability	10^{-13} m ²
η	Fluid viscosity	10^{-3} Pa·s
α	Hydraulic diffusivity	0.1 m ² /s
l_f	Half-length of rate-and-state fault	20 km
Δz	Suggested cell size	10 m
t_{off}	Injection turn-off time	100 days
t_f	Final simulation time	2 years
Parameters for BP6-A/S		
a	Rate-and-state direct effect parameter	0.007
b	Rate-and-state evolution effect parameter	0.005
D_{RS}	State evolution distance	4 mm
V_*	Reference slip rate	10^{-6} m/s
f_*	Reference friction coefficient	0.6
V_{init}	Initial slip rate	10^{-12} m/s
Parameters for BP6-C		
f	Coefficient of friction	0.6
V_{init}	Initial slip rate	0 m/s

3.1.2. BP6-QD-C: Constant Friction

For BP6-QD-C, the coefficient of friction f is constant and the shear resistance $F(p)$ depends only on the change in pore fluid pressure p . With constant friction, we distinguish between locked and slipping states of the interface. When the shear stress is lower than the shear resistance, the fault is locked and the shear stress is given by the sum of the reference shear traction and the shear stress change due to quasi-static deformation:

$$\tau = \tau^0 + \Delta\tau, \quad \tau < F(p), \quad V = 0. \quad (7)$$

When the fault is sliding, the shear stress is equal to the shear resistance:

$$\tau = \tau^0 + \Delta\tau - \frac{\mu}{2c_s}V, \quad \tau = F(p), \quad V > 0. \quad (8)$$

Analytic or semi-analytic solutions exist for problems similar to BP6-QD-C considering slip with constant friction under a constant fluid volume injection rate (Saez et al., 2022) and constant pore pressure at the injection site (Jacquey & Viesca, 2023; Viesca, 2021).

Note that the constant friction coefficient f for BP6-C is chosen to be the same as the reference friction coefficient $f_* = 0.6$ for the rate-and-state problems BP6-QD-A/S under steady-state sliding at the reference slip rate $V_* = 10^{-6}$ m/s (Table 3). However, the sliding friction differs for the rate-and-state models when the slip rate differs from steady slip at the reference slip rate.

3.2. Fluid Injection and Along-Fault Diffusion

Fault slip is induced by perturbations in pore fluid pressure due to fluid injection at the center of the fault $z = 0$ and along-fault fluid diffusion. The evolution of pore fluid pressure along the fault can be expressed by the 1-D pressure diffusion equation:

$$\frac{\partial p}{\partial t} = \frac{k}{\phi\beta\eta} \frac{\partial^2 p}{\partial z^2} + \frac{q_{\text{inj}}(t)}{\beta\phi} \delta_D(z). \quad (9)$$

Here we assume constant and spatially uniform permeability k , fluid viscosity η , rock porosity ϕ , and compressibility β . The effects of gravity are neglected and we assume zero fluid flux (i.e., $\partial p/\partial z = 0$) outside of the frictional domain Ω_f . Fluid flow is confined to the fault, with fault-normal flow neglected.

The last term on the right-hand-side of Equation 9 represents the fluid source term with $q_{\text{inj}}(t)$ being the fluid injection rate (volume per time, per unit area in the x-y plane) and $\delta_D(z)$ is the Dirac delta function. Fluid injection occurs at a constant injection rate q_0 for time interval $0 \leq t < t_{\text{off}} = 100$ days, after which fluid injection is turned off (Figure 1). For the specific problem, the evolution of pore pressure approximately follows the analytic solution for injection into an infinite fault (provided in the Supporting Information S1; Carslaw & Jaeger, 1959). BP6-QD considers the evolution of fault slip due to these transient pore pressure perturbations over a total simulation period of 2 years.

All parameters for the suite of benchmark problems BP6-QD-A/S/C are given in Table 3. Fault frictional parameters, including initial effective normal stress and rate-and-state properties, are motivated by laboratory friction experiments of granite around hydrothermal conditions for typical seismogenic depths considering some fluid overpressure (Blanpied et al., 1991, 1995), as well as considerations of numerical resolution and computational expense based on prior modeling studies (Section 3.3; Erickson et al., 2020; Erickson et al., 2023; Jiang et al., 2022). For example, laboratory values of the characteristic slip distance D_{RS} are typically on the order of microns, however we choose a value several orders of magnitude larger for computational tractability. Fluid

transport properties such as fault zone permeability can vary widely depending on lithology and deformation history (Allègre et al., 2016; Cappa et al., 2019, 2022a, 2022b; Guglielmi et al., 2015, 2021; Xue et al., 2016). The values chosen for fault zone permeability, porosity, and (pore and fluid) compressibility in BP6 are consistent with those determined from in situ well measurements for densely fractured sandstone near the Happy Valley and San Andreas Fault zones (Allègre et al., 2016; Xue et al., 2016), as well as reservoir modeling of fluid injection in a granite fault zone (Llanos et al., 2015). Complete details, including initial and boundary/interface conditions, are included in Supporting Information S1 and on our online platform.

3.3. Considerations of Computational Domain Size and Spatial Discretization

The frictional domain $\Omega_f = (-l_f, l_f)$ in BP6-QD is specified as a 40-km region (Table 3) and the elastic medium is considered to be an infinite whole-space. The majority of the participating codes in BP6-QD (Tables 1 and 2) are required to make choices for finite computational domain lengths that sufficiently capture the response of the whole-space. The exceptions to this are the BEM-based codes (QDBIM and HBI) that only consider the rate-and-state frictional section of the fault Ω_f , with implicit consideration of zero slip outside of Ω_f and far-field displacements $u \rightarrow 0$ as $x \rightarrow \infty$.

For the SBEM codes (BICycle and FastCycles), the fault is discretized along a finite length L_z (z -direction) and subject to periodic boundary conditions, defining a region referred to as a replication cell. The slip and slip rate are prescribed to be zero on both sides of the replication cell outside of Ω_f for BP6-QD to approximate the zero displacement boundary conditions. In practice, calculation of the elastic stress transfer in the Fourier domain introduces an infinite number of fault segments of multiples of L_z , which must be sufficiently large (compared to Ω_f or the slip domain of interest) to minimize the interaction among the replicated frictional segments. FEBE, which is a hybrid SBEM/FEM code, also chooses L_z in the same manner as the pure SBEM codes. The SBEM code of (Dublanchet, 2019) implements elastic stress transfer kernels in the Fourier domain that remove the effects of spatial replications (Cochard & Rice, 1997) and more accurately implements the zero displacement boundary conditions. While effectively removing the periodic boundary conditions, the model domain L_z must be at least twice as long as the frictional domain of interest to capture the stress transfer solution.

Volume-based codes (GARNET, Thrash, Scycle and Tandem) must discretize a 2-D domain and determine values for both spatial dimensions L_z and L_x (x -direction) that are sufficiently large to approximate the response of an infinite elastic domain. The inclusion of a volume discretization provides increased flexibility to consider more complex material properties (e.g., heterogeneities, inelasticity), however such methods are inherently more computationally expensive than those based on BEM. To ease computations, volume-based codes can employ grid stretching, where higher resolution can be localized in a region around the fault and the mesh coarsens away from the frictional domain (as discussed in][and references in Table 1 Erickson et al., 2023).

In our prior benchmark comparisons, we found simulated outcomes from SEAS models can quantitatively and even qualitatively differ depending on the choice of a finite computational domain size to approximate an infinite or semi-infinite space (Erickson et al., 2020, 2023; Jiang et al., 2022). In addition to finite computational domain size, far-field boundary conditions must also be chosen, with displacement or traction-free conditions being common choices across modeling groups employing a volume discretization. Our prior comparisons revealed that simulated results eventually converge for sufficiently large domain sizes, at which point the results also did not show a strong dependence on the type of remote boundary condition. For BP6-QD, we also find that the choice of boundary conditions can result in mild differences in the simulated fault slip behavior, which diminishes for larger computational domains. The model domain sizes and boundary conditions used for participating codes are summarized in Table 2 and we further discuss their implications for our comparisons in Section 4.4.

Requirements on spatial discretization in our prior benchmark comparisons included resolving important physical length scales. Such important scales in SEAS models include the process zone Λ , which describes the spatial region near the rupture front under which breakdown of fault resistance occurs (Palmer & Rice, 1973), and the critical nucleation scale h^* , which governs the minimum extent of the rate-and-state velocity-weakening region in which spontaneous nucleation of frictional instability may occur (Dieterich, 1992; Rice & Ruina, 1983). For BP6-QD-A/S, the rate-and-state fault models are governed by purely VS friction which precludes spontaneous nucleation, and hence the need to consider h^* .

As guidance for adequate spatial resolution, we consider estimates of the process zone size given the parameter values in BP6-QD (Table 3). For rate-and-state fault models with constant effective normal stress $\bar{\sigma}$ and governed by the aging law formulation of state evolution, the quasi-static process zone at a rupture speed of 0^+ , Λ_0 , can be estimated (Ampuero & Rubin, 2008b; Day et al., 2005; Perfettini & Ampuero, 2008) as:

$$\Lambda_0 = C \frac{\mu^* D_{RS}}{b \bar{\sigma}}, \quad (10)$$

in which C is a constant of order 1 and μ^* is the effective stiffness of the surrounding material ($\mu^* = \mu$ for antiplane strain). Simulations using the slip law formulation for the state variable evolution have found that the quasi-static process zone can be 10–20 times smaller than the estimate of Λ_0 using the aging law (Ampuero & Rubin, 2008b).

For BP6-QD, we suggest a computational cell size of 10 m based on the estimate of $\Lambda_0 \approx 450$ m using Equation 10 and consideration of the need for finer discretization to resolve the more rapid state evolution with the slip law in BP6-QD-S. Results from most participating codes use the suggested cell size of 10 m, however some of the volume-based codes submitted results for larger cell sizes (Table 2). Note that for numerical methods (such as high-order FEM) that are not based on equally spaced grids, cell size should be interpreted as an average resolution per degree of freedom along the face of an element. For BP6-QD-A and BP6-QD-S, we find that the submitted results of differing cell sizes all agree well by both visual inspection and our quantitative metrics, as discussed in more detail in Section 4. We find that more notable differences in the presented solutions can be attributed to domain size effects and choices in time-stepping.

3.4. Methodologies for Pore Pressure Evolution and Time-Stepping

Participating modeling groups implement changes in pore fluid pressure throughout simulations of BP6-QD either by solving Equation 9 numerically or by imposing the analytic pore pressure solution along the fault at each time step. Codes that numerically solve for the evolution of pore fluid pressure implement different integration techniques, including explicit (e.g., forward Euler) and implicit (e.g., backward Euler) integration methods, as summarized in Table 2. Implicit methods require more involved computations but allow for more stable solutions with larger time steps, whereas explicit methods can require smaller time steps to ensure numerical stability.

An important ingredient of most SEAS simulations is the use of adaptive time stepping to efficiently resolve extended periods with varying rates of motion and other physical processes. A subset of our participating codes (BICyclE-1 and -2, GARNET, and FEBE) implement the adaptive time-stepping methodology of (Lapusta et al., 2000), which adopts a new time step based on frictional stability considerations of the rate-and-state properties. The adaptive time step is determined to be inversely proportional to the current slip rate such that periods of faster motion require finer temporal sampling. Importantly for BP6-QD, the stability considerations for the adaptive time step do not directly consider changes in fault shear resistance due to changes in effective normal stress or pore fluid pressure.

Most of the remaining codes adopt high-order accurate (4/3 or 4/5), adaptive, explicit RK methods. Such RK methods are used for numerical integration, with adaptive time-stepping executed by estimating the local truncation error based on two numerical solutions of differing orders of accuracy. Specific methods (e.g., Dormand-Prince RKDP45 and Fehlberg RKF45) can differ in terms of which order estimates are used to calculate the truncation error and produce the solution at the new time step. The SBEM code FastCycles implements an RK-like time-stepping scheme by using error control on solution estimates computed for one full time step Δt as well as two successive half time steps $\Delta t/2$ (Romanet & Ozawa, 2021). As RK methods are not motivated by the conditions of a specific physical problem, they can readily consider the evolution of multiple physical quantities, such as the frictional state variable, slip, shear stress and pore fluid pressure, when determining appropriate temporal resolution for solving coupled equations. While some codes apply explicit error control on only select quantities, such as the frictional state variable and shear stress, the effects of other quantities may be implicitly considered in the error estimates of coupled processes.

All of the participating codes implement an adaptive time-stepping framework, however some (BICyclE-2 and Scycle) apply a further restriction on the maximum time step of 500 or 1000s in order to ensure that the evolution

of pore fluid pressure is adequately resolved. This choice of maximum time step is motivated by the characteristic fluid diffusion time across a computational cell ($t_{\text{diff}} \propto \Delta z^2/\alpha = 1000$ s for $\Delta z = 10$ m and diffusivity $\alpha = 0.1$ m²/s from Table 3). A summary of the time-stepping methodologies used by participating codes is available in Table 2.

3.5. Quantitative Metrics

In addition to our visual assessment of model comparisons, we define quantitative metrics for comparing simulated quantities. First, to compare the resolved pore pressure distributions we compute the L^2 -norm (integrated-) error in pore pressure time series at specific locations along the fault for each simulation relative to the analytic solution (provided in Supporting Information S1). The analytic pore pressure distribution is computed at the corresponding temporal output for each simulation and the relative error (expressed as a percent), is defined by

$$\% \text{ err}(P) = \|P_{\text{ana}} - \tilde{P}\| / \|P_{\text{ana}}\| \times 100, \quad (11)$$

where the norm is defined for a fault variable g at a specific location by $\|g\|^2 = \int_0^T |g(t)|^2 dt$, with $T = 2$ years (i.e., the full simulation period), and integrals are approximated with trapezoidal quadrature.

We choose a reference solution from our participating codes to assist in quantitatively comparing the simulated slip history results from different codes. The BEM solution of QDBIM is chosen as a reference solution for problems BP6-QD-A and BP6-QD-S, given the exact consideration of an infinite elastic domain and the boundary conditions of the mathematical problem. Simulation results using a cell size of $\Delta z = 5$ m were chosen for the reference solution based on self-convergence tests demonstrating consistent solutions with further mesh refinement (Figure S1 in Supporting Information S1).

As a quantitative metric for comparing the resolved slip history across simulations we compute the L^2 -norm (integrated-) error in slip-rate time-series at specific locations along the fault. In order to compare both the arrival timing and the shape of the slip rate pulse, we first align the slip velocity time series from a certain model with the reference solution by finding the best time shift that maximizes the cross-correlation of the two time-series. If $V_{\text{ref}}(t)$ and $\tilde{V}(t)$ are the reference and (shifted) comparative slip rates respectively, we then compute the relative error as:

$$\% \text{ err}(V) = \|V_{\text{ref}} - \tilde{V}\| / \|V_{\text{ref}}\| \times 100. \quad (12)$$

As the amplitude and width of the slip rate pulse varies considerably at different points along the fault, we define the period T for both the cross-correlation and norm at each point by (a) identifying the peak slip rate at each point of the reference solution and (b) determining the duration of the pulse between when the slip rate exceeds and drops below half of the peak slip rate. We then define T to be the maximum of either 1 s or four times the width of slip pulse in the reference solution, such that the cross-correlation and norm at each point are calculated over the period representing two pulse widths before and after the peak slip rate of the reference solution. The resulting time shifts that maximize the cross-correlation between the reference and comparative slip rates also provide a measure of the difference in slip rate arrival time at different fault locations.

To compare the final slip distributions from each simulation we also calculate the percent error between the slip value δ_{fin} at time $t = 2$ years for different fault positions relative to the reference solution:

$$\% \text{ err}(\delta^{\text{fin}}) = |\delta_{\text{ref}}^{\text{fin}} - \tilde{\delta}^{\text{fin}}| / |\delta_{\text{ref}}^{\text{fin}}| \times 100. \quad (13)$$

Given the different choices in adaptive time step across simulations, the calculation of percent variation in simulated quantities through trapezoidal quadrature can be sensitive to the number and resolution of time steps for each time series. Prior to computing the percent variation for a given quantity, we interpolate the time series from each simulation to use consistent temporal discretization during trapezoidal quadrature. To examine the sensitivity of our quantitative metrics to the temporal sampling of individual simulations we compare the percent variation in slip rate for time series data with varying degrees of temporal downsampling. We downsample the slip velocity time series data at different fault locations by factors of 1 (not downsampled), 2, 3 and 4, then

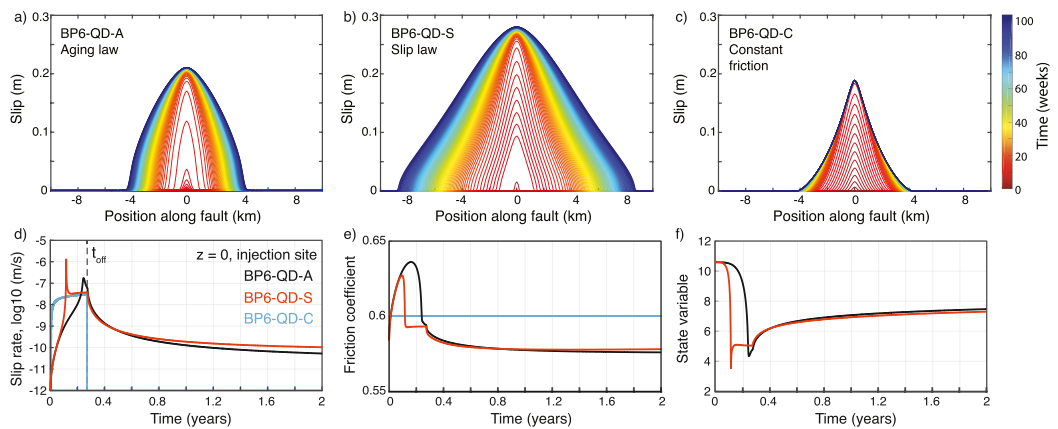


Figure 2. Problem BP6-QD-A/S/C considers the evolution of an aseismic slip transient under different treatments of fault friction, including rate-and-state models using the (a) aging and (b) slip law formulation of the frictional state evolution, and (c) a constant friction coefficient (Results from BICyclE-1, contoured weekly). Given the same time-dependent perturbation in pore fluid pressure, the evolution of slip across the three problems substantially varies. (d)–(f) Time series evolution of the local slip rate (d), friction coefficient (e), and state variable $\psi = \log(\theta V^*/D_{RS})$ at the injection site ($z = 0$ m). Both rate-and-state models exhibit an initial delay in slip acceleration with fluid pressurization (d) due to the direct strengthening of friction with increased slip velocity (e). Results from BP6-S exhibit faster slip acceleration compared to BP6-A given the more rapid state variable evolution using the slip (vs. aging) law (f), and hence reduction in frictional resistance (e). For BP6-C, slip initiates more rapidly (e) during fluid injection and quickly arrests upon injection shut-off as the fault shear resistance directly follows changes in pore pressure with no friction evolution (f).

perform the interpolation of the downsampled data to the same fixed time step and calculate the percent variation with respect to the reference BEM solution. The results of these comparisons are shown in Figure S2 in Supporting Information S1 for 5 participating codes (BICyclE-1, QDBIM, Garnet, Thrace, and Tandem) that use different numerical methodologies and time-stepping strategies. The difference between the percent variation in slip rate for downsampling factors up to a factor of 4 are within 0.1%, which is an order of magnitude lower than the differences determined between codes (Section 4). This comparison suggests that the temporal sampling for the submitted simulation results is sufficiently fine for our quantitative metrics to predominantly reflect differences in simulation results across codes, rather than differences in trapezoidal quadrature due to temporal sampling.

4. Comparisons of Simulation Results

The evolution of slip notably varies across simulations of the three benchmark problems BP6-QD-A/S/C with different treatments of fault friction, given the same time-dependent perturbation in pore fluid pressure (Figures 1 and 2a–2c). Both rate-and-state models exhibit slow initial slip acceleration with fluid pressurization due to the initial strengthening of friction with increased slip velocity via the direct effect (Figures 2d and 2e). Results from BP6-QD-S exhibit faster slip acceleration compared to BP6-QD-A given the more rapid state variable evolution using the slip (vs. aging) law, and hence reduction in frictional resistance from the peak friction (Figures 2e and 2f). For BP6-QD-C, slip initiates more rapidly during fluid injection but quickly arrests upon injection shut-off as the fault shear resistance directly follows changes in pore pressure with no friction evolution. For both rate-and-state models, the peak slip rate tends to precede the peak change in pore fluid pressure at various fault positions, indicating that the aseismic slip front outpaces the pore pressure diffusion front due to the elastic stress transfer (Figures 3 and 4, e.g. Bhattacharya & Viesca, 2019).

For the parameter values chosen, both rate-and-state models (BP6-QD-A/S) result in greater average slip during the aseismic transient compared to the model with constant friction (BP6-QD-C), with the fault model using the slip law resulting in even more pronounced slip and approximately twice as large of a slipped area over the two-year simulation period compared to the other two models using the aging law or constant friction. This result is likely due in part to the different sliding friction coefficients in the interior of the aseismic rupture (Figure 2e). As the slip rate at points within the interior of the aseismic rupture is lower than the reference slip rate $V_* = 10^{-6}$ m/s (Figure 2d), the corresponding sliding friction for both VS fault models is lower than the reference friction

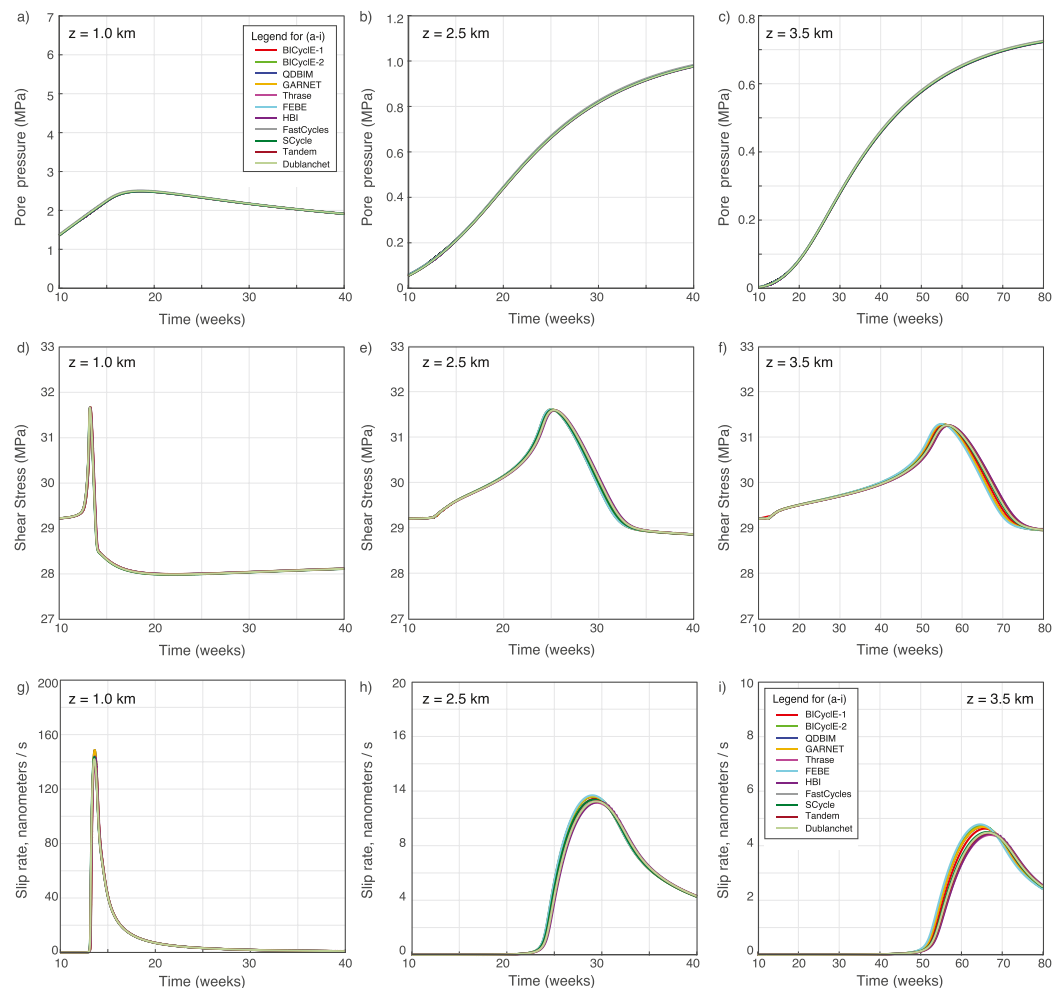


Figure 3. Time series evolution of local pore fluid pressure (a)–(c), shear stress (d)–(f), and slip rate (g)–(i) at different points along the fault for simulations of BP6-QD-A using the aging law.

$f_* = 0.6$, and hence the specified friction coefficient for BP6-QD-C (Figure 2). Thus, given the same initial shear stress, the differing sliding frictions result in larger stress drop, slip, and propagation speeds for the rate-and-state fault models (BP6-QD-A/S) compared to the case with a constant friction coefficient (BP6-QD-C). The more pronounced aseismic rupture growth using the slip law (vs. aging law) is also consistent with the concept that the rate-and-state friction law provides a larger effective fracture energy using the aging law compared to the slip law, and hence results in greater resistance to initial rupture growth (Ampuero & Rubin, 2008b; Garagash, 2021).

In the following, we discuss results from our community comparisons of simulations for rate-and-state fault problems BP6-QD-A and BP6-QD-S, for which solutions have been collected from a number of participating groups. Simulations results from participating modeling groups for the two benchmark problems as well as BP6-QD-C with constant friction are available on our online platform.

4.1. Evolution of Fault Pore Fluid Pressure

As benchmark problem BP6-QD incorporates one-way coupling between changes in pore fluid pressure and fault slip, we begin by comparing simulated results for the pore fluid pressure evolution across participating codes for BP6-QD-A and BP6-QD-S. We find that the time series evolution of pore fluid pressure at different fault locations from all participating codes is virtually identical upon visual inspection (Figures 5a–5d). Comparison of our quantitative metric in terms of the percent error in time-integrated pore pressure at varying fault positions reveals excellent agreements in simulated pore pressure evolution, within 1% of the analytic solution, for results for both problems BP6-QD-A and BP6-QD-S (Figures 5e and 5f). Note that the percent error in simulated pore pressure

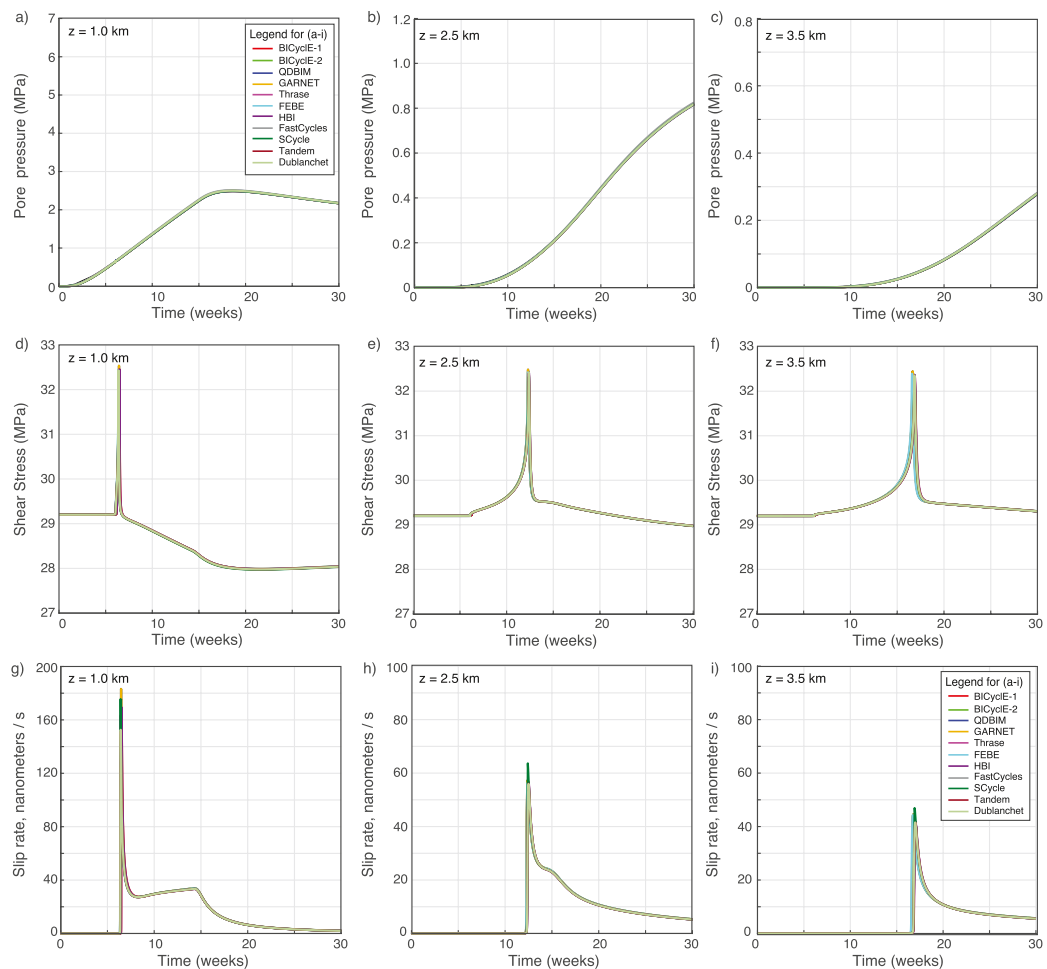


Figure 4. Time series evolution of local pore fluid pressure (a)–(c), shear stress (d)–(f), and slip rate (g)–(i) at different points along the fault for simulations of BP6-QD-S using the slip law. Results from BP6-QD-S using the slip law result in more pronounced slip acceleration, including higher peak slip rate and more temporal localization of slip and shear stress at the slip front, compared to BP6-QD-A models using the aging law (Figure 3).

evolution tends to be higher at points near the injection site where larger gradients in pore pressure change also lead to more rapid changes in pore pressure (Equation 9, Figures 5e and 5f).

4.2. BP6-QD-A Model Comparisons

Comparisons of benchmark problem BP6-QD-A using the aging law show good agreement among simulation results from participating codes upon visual inspection, as illustrated by the close overlap of shear stress and slip rate time series in Figure 3. More refined visual inspection of the different results reveals slight offsets in the arrival times (within 1 week) of the aseismic slip fronts between simulations from different codes (Figures 6a and 6b).

One group of simulation results (denoted Group 1 including BiCycle-2, QDBIM, Thrase, FEBE, FastCycles, SCycle, Tandem, and Dublanchet) show close agreement in the slip rate and shear stress time series evolution at points closer to the injection site earlier on in the simulated aseismic transient (Figure 6a). Another group of results (denoted Group 2, including BiCycle-1, GARNET, and HBI) exhibits a slight lag compared to the results of Group 1 at points closer to the injection site.

Similarly, a cluster of simulation results (denoted Group 3 including QDBIM, Thrase, FastCycles, SCycle, HBI, Tandem, and Dublanchet) show close agreement in local simulated time series data at points further away from the injection site and periods later on in the simulated aseismic transient (Figure 6b). Results from the remaining

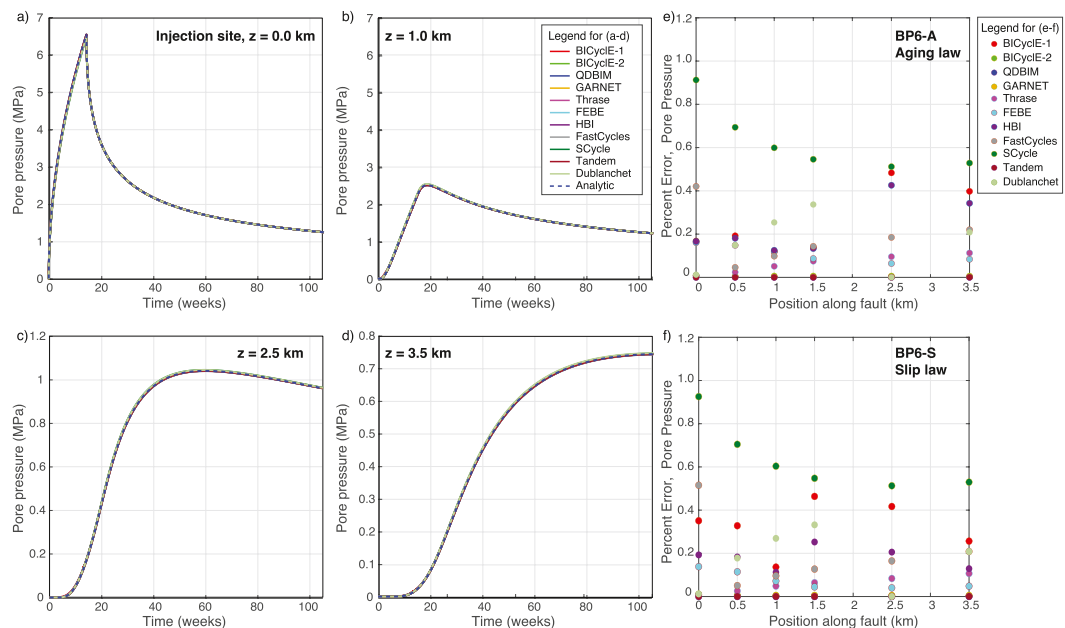


Figure 5. Comparison of time series evolution of fault pore fluid pressure at different fault locations (a)–(d) with respect to the analytic solution (blue dashed line), shown here for simulations of BP6-QD-A. (e)–(f) The percent error for the pore pressure evolution with respect to the analytic solution is computed at different fault positions for each simulation result for (e) BP6-QD-A and (f) BP6-QD-S.

codes (denoted Group 4 including GARNET, BIcycle-1, BIcycle-2, FEBE) show slightly earlier arrival of the slip transient at points further from the injection site compared to the result in Group 3. Note that codes included in Groups 1 and 3, and similarly Groups 2 and 4, show some overlap but are not identical.

These grouping and shifts in relative slip front arrival times are evident in our quantitative metric comparisons of the cross-correlation lags from the simulated slip rate time series at different fault positions (Figure 7). The cross-correlation lags show consistent timing for results from Group 1 with the reference BEM solution (QDBIM is in Group 1), with Group 2 showing delayed time offsets (within 0.1 weeks variation) at points closer to the injection site (Figure 7c). Similarly, Group 3 results show consistent timing with the reference BEM solution, while Group 4 results show earlier arrivals (within 0.2 weeks variation) at points further from the injection site. Once the slip rate time series are aligned using the cross-correlation lags, comparison of the percent error in time-integrated slip rate show generally good agreement between the resolved slip rate time functions, within 6% variation about the reference BEM solution (Figure 7e). Similarly, the overall slip evolution at different fault positions shows good agreement across simulations, with the percent variation in final slip being generally within 6% of the reference solution and within 2% variation for most results, particularly at points closer to the injection site (Figures 8a–8c).

4.3. BP6-QD-S Model Comparisons

Similar to BP6-QD-A, comparisons of results from BP6-QD-S using the slip law reveal generally good agreement across simulations from participating codes upon visual inspection (Figure 4), with small differences in the aseismic slip front arrival time (within 1 week) upon more refined inspection (Figures 6c and 6d). The grouping of results for different codes (Groups 1–4) is consistent between simulations of BP6-QD-A and BP6-QD-S, though the variations in slip front arrival timing and slip time series evolution are greater for results of BP6-QD-S using the slip law (Figures 7c and 7e vs. 7d and 7f).

Codes in Groups 1 and 3 exhibit consistent timing with the reference BEM solution, as quantified by the cross-correlation lags from the slip rate time series (Figure 7d). Results from Group 2 show delayed arrival of the slip front (within 0.15 weeks) compared to the reference solution at points closer to the injection site, and results from Group 3 exhibit slightly earlier slip front arrivals (within 0.3 weeks) at points further from the injection site. The percent error in the time-integrated slip rate of the aligned time series shows greater variation in slip rate evolution

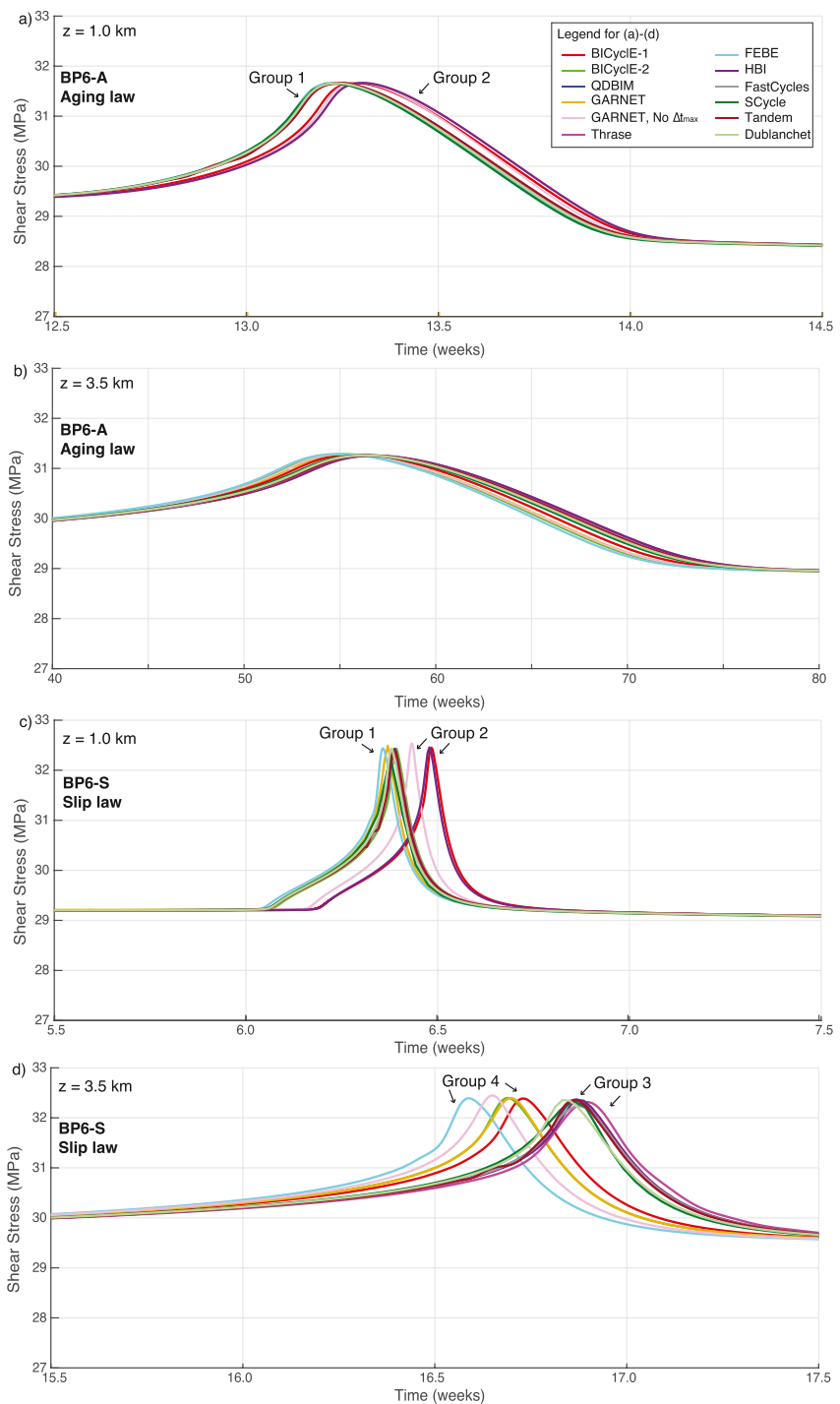


Figure 6. Zoomed in comparison of the shear stress time series evolution at different points in BP6-QD-A (a)–(b) and BP6-S (c)–(d). A grouping of the simulation results show comparable timing in peak shear stress arrival at the rupture front, with initial results from a few codes (BICycleE-1, GARNET, and HBI) showing slightly delayed arrival earlier on in the aseismic transient ($z = 1 \text{ km}$, (a) and (c)), and another set of codes (BICycle-1, BICycle-2, GARNET, FEBE) showing earlier arrival of the slip front later on in the simulation ($z = 3.5 \text{ km}$, (b) and (d)).

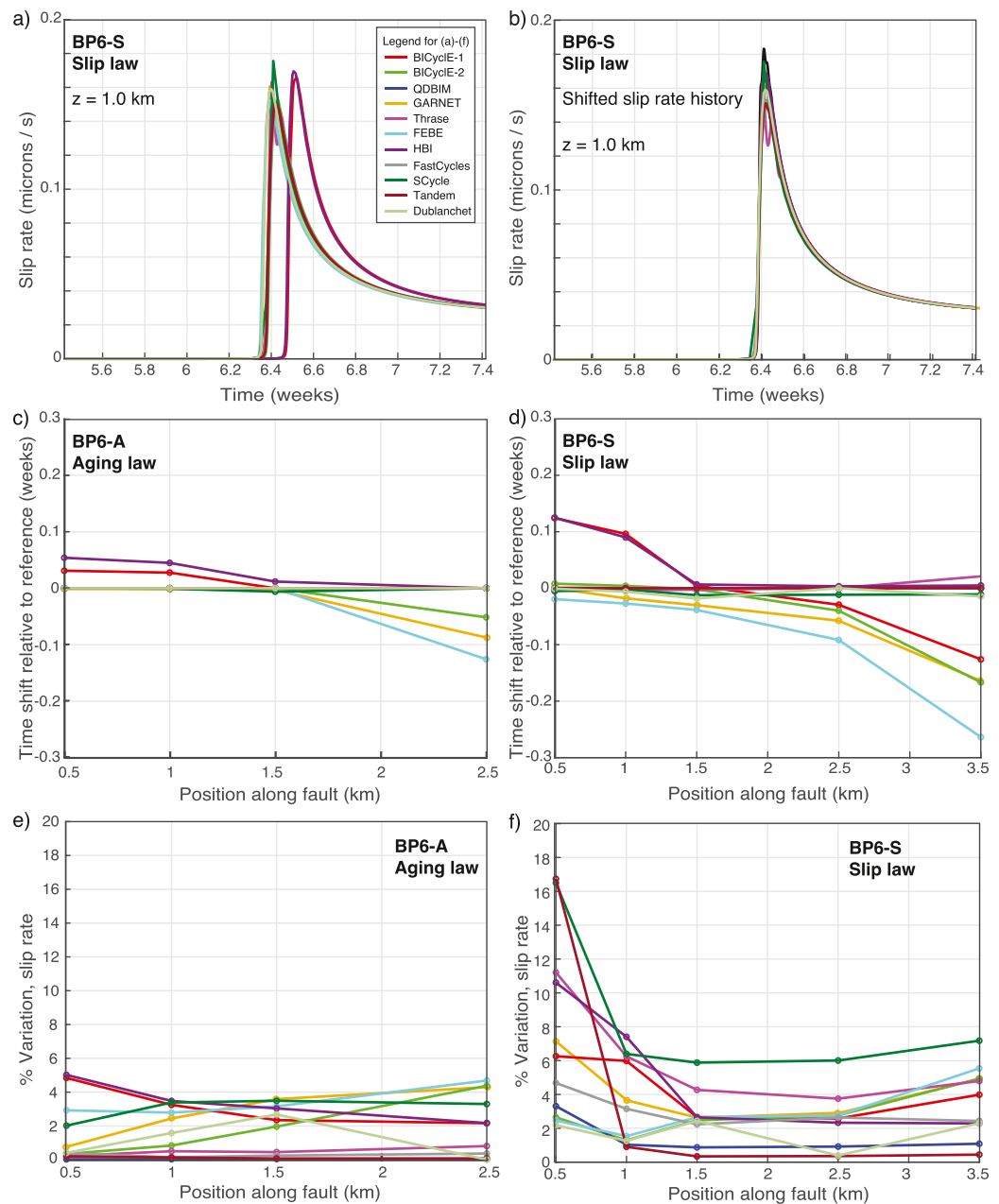


Figure 7. Quantitative metric comparisons of slip rate evolution for BP6-QD. Slip rate times series at different points along the fault are cross-correlated with a reference boundary element method (BEM) solution (QDBIM) to determine appropriate time shifts to minimize relative error, as shown for (a) BP6-A and (b) BP6-S. The slip rate time series are then aligned using the time shifts (c)–(d) and the percent variations against the reference solution are computed for different fault positions (e)–(f).

for simulations of BP6-QD-S compared to BP6-QD-A (up to 18% variation for BP6-QD-S vs. 6% for BP6-QD-A, Figures 7e and 7f), however the percent variation for most results are within 6% of the reference BEM solution. The highest percent errors in time-integrated slip rate occur for fault locations closer to the injection site ($|z| < 1.5 \text{ km}$), potentially reflecting the higher gradients in pore fluid pressure change near the injection site (Figures 5a and 5b vs. 5c and 5d) which also couple with the more rapid evolution of the frictional state variable and fault slip using the slip law. The overall slip evolution at different fault positions show good agreement across simulations for BP6-QD-S, with percent error in final slip generally within 6% of the reference solution and even lower variation within 3% at points closer to the injection site ($|z| < 1.5 \text{ km}$). The variations in final slip across different

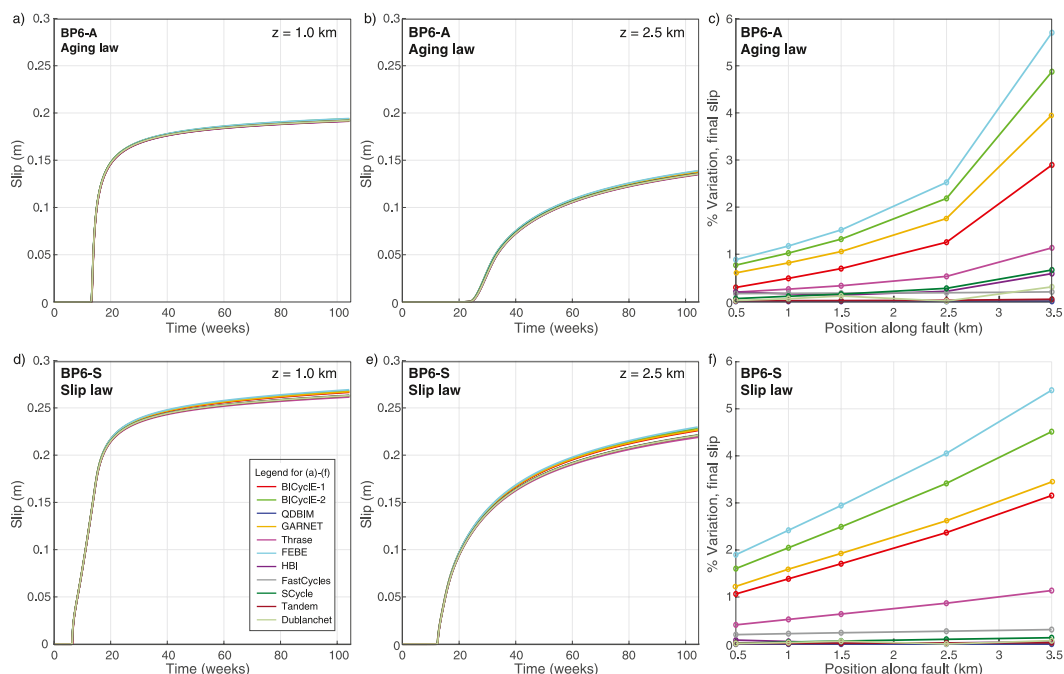


Figure 8. Comparison of slip time series evolution at different fault positions ($z = 1$ km and $z = 2.5$ km) for simulations of BP6-QD-A (a)–(b) and BP6-QD-S (d)–(e). Percent errors in the final slip values at $t = 2$ years are computed at different fault positions against the reference BEM solution (QDBIM) (c) and (f).

simulation results for BP6-QD-S are generally comparable to, though slightly greater than those observed for results of BP6-QD-A (Figures 8d–8f vs. 8a–8c).

4.4. Reducing Discrepancies in Simulations of BP6-QD-A and BP6-QD-S

We find that initial simulation results from participating codes for both BP6-QD-A and BP6-QD-S generally agree well upon visual inspection. The most notable discrepancies between the simulation results are the groupings of codes (Groups 1–4) that show different arrival times and evolution of the aseismic slip transient at points closer to the injection site (Groups 1 vs. 2) and further from the injection site (Groups 3 vs. 4).

We note that the three codes in Group 2 that exhibit a slight lag in the aseismic slip front (compared to Group 1) at points close to the injection site all numerically solve for pore pressure evolution using implicit integration methods, which allow for more stable pore pressure solutions with longer time steps. Two of the codes (BICycle-1 and GARNET) utilize the time-stepping method of (Lapusta et al., 2000) with no specific time step restriction based on the pore pressure evolution. HBI uses a 4/5th-order RK method with error control on the frictional state variable and shear stress. The codes in Group 1 utilize different adaptive time-stepping methods including high-order RK methods as well as the methodology of (Lapusta et al., 2000). However, the results of SBEM code BICycle-2 (in Group 1), which use the methodology of (Lapusta et al., 2000) and explicit numerical integration of the pore fluid pressure evolution, also implement additional restrictions on the maximum allowed time step based on considerations of the characteristic time scale for pore pressure diffusion.

We further examine results from SBEM code BICycle-1, which implements implicit pore pressure integration with time step considerations based on (Lapusta et al., 2000), and review how the simulation results vary with an imposed maximum time step Δt_{\max} (Figures 9a and 9d). We compare the results with different maximum time step restrictions (no Δt_{\max} restriction, $\Delta t_{\max} = 1000$ s, and $\Delta t_{\max} = 500$ s) to the reference BEM solution (QDBIM) which uses RK45 adaptive time-stepping with explicit error control on the pore pressure evolution. We find that implementing a maximum time step restriction of 1,000 or 500 s in the SBEM code improves the agreement with the reference BEM solution for the time series evolution of local fault quantities closer to the injection site in both BP6-QD-A and BP6-QD-S (Figures 9a and 9d). The finer temporal sampling improves the agreement between the simulated pore pressure evolution and the analytic solution, reducing the percent error to around or below 0.01%

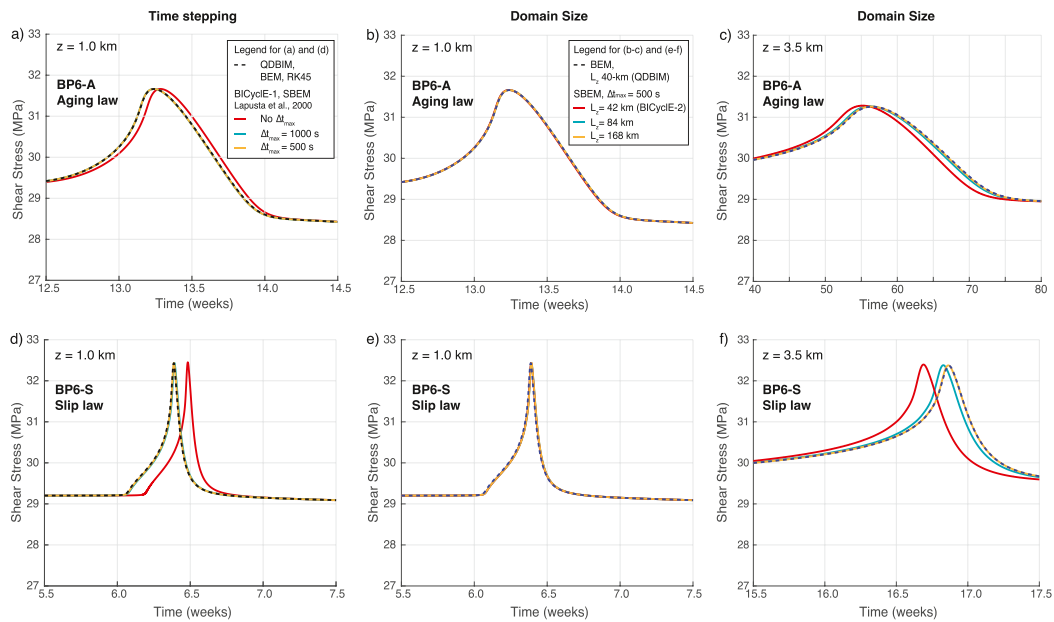


Figure 9. Comparison of shear stress evolution for boundary element method, BEM and spectral boundary element method, SBEM simulations with different time-stepping and model domain size. (a) The shear stress evolution at the slip front in SBEM simulations BP6-QD-A using the time-stepping method of (Lapusta et al., 2000) (red) lags slightly behind the BEM solution using RK45 time stepping (dashed black). The discrepancy is reduced by implementing a maximum time step Δt_{\max} of 500 s (yellow) or 1,000 s (blue) in the SBEM simulations (blue line behind yellow and dashed-black in (a)–(b) and (d)–(e)). (b)–(c) Sufficiently fine temporal sampling results in comparable SBEM and BEM solutions early on in the simulations of BP6-QD-A (b, $z = 1$ km), however the shear stress peak arrives slightly earlier in the SBEM solution with a model domain of $L_z = 42$ km (c, $z = 3.5$ km, red vs. black). The SBEM solution becomes more consistent with the BEM solution as the model domain size is increased. (d)–(f) Similar comparison for choices in (d) time-stepping and (e)–(f) model domain size for BP6-QD-S using the slip law.

(Figures 10a and 10e). Refining the temporal resolution of the pore pressure evolution has a more notable effect on the slip behavior for points closer to the injection site, likely due to the much larger gradient and hence temporal variation (Equation 9) and absolute error in the pore pressure change distribution (Figures 9 and 10).

While refining the temporal discretization improved the alignment of the SBEM and reference BEM results closer to the injection site, it had marginal effect on the greater discrepancy in the slip front arrival time and overall slip evolution at points further from the injection site (Figure 10). In fact, the finer temporal sampling resulted in slightly more pronounced slip, which compounded into slightly increased variability in the final slip and slip evolution at points further from the injection site compared to the reference solution for BP6-QD-A (Figures 10c and 10d).

We performed another series of tests using the SBEM code BICyclE with a maximum time step of 500 s and varying the computational domain size (replication cell L_z) for BP6-QD-A (Figures 9b–9d) and BP6-QD-S (Figures 9e and 9f). We find that results for SBEM simulations using sufficient temporal resolution and different computational domain sizes show highly comparable time series evolution of local shear stress and slip rate at points close to the injection site ($|z| < 1.5$ km), with percent error in time-integrated slip rate and final slip within 3% of the reference BEM solution (Figure 10). However, the timing and overall evolution of local slip and shear stress at points further from the injection site ($|z| > 2$ km) show a greater dependence on the computational domain size for SBEM simulations (Figures 9c, 9f and 10). Increasing the SBEM replication cell L_z from 42 to 168 km substantially improves the agreement between the SBEM and reference BEM solutions, resulting in virtually identical aseismic slip arrival times (Figures 10b and 10f), and reducing the percent variation in integrated slip rate and final slip from up to 5% error at different fault positions for $L_z = 42$ km to less than 1% error at almost all points for $L_z = 168$ km (Figures 10c, 10d, 10g and 10h). Note that the increased variation in final slip at points further from the injection site for both BP6-QD-A/s is likely due to both the influence of effects from the finite domain size and choices in remote boundary conditions, as well as the accumulation of differences in slip across the entire rupture history, with the combined effects becoming less pronounced with increased computational

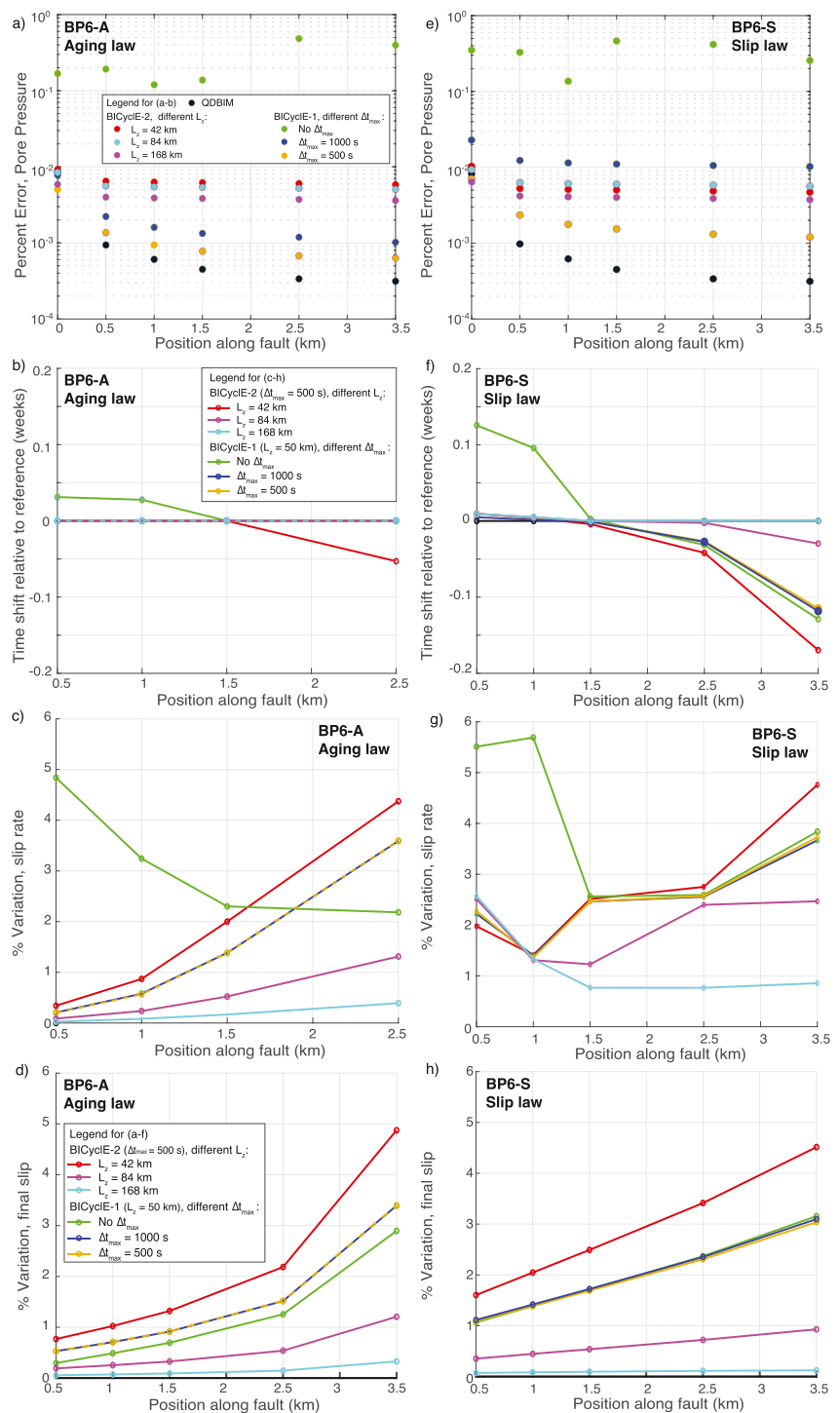


Figure 10. Quantitative metric comparison for SBEM simulations with different model domain sizes and constraints on maximum time step for BP6-QD-A (a)-(c) and BP6-QD-S (d)-(f). Dashed lines are shown for colored lines that overlap. (a and e) The percent error in time-integrated pore pressure is calculated at different points along the fault with respect to the analytic solution. The slip rate times series at different points along the fault are cross-correlated with a reference boundary element method, BEM solution (QDBIM) to determine appropriate (b) and (f) time shifts to minimize relative error, and then the percent errors in integrated slip rate are computed against the reference solution (c) and (g). (d) and (h) Percent errors for the final slip values at $t = 2$ years are computed at different fault positions against the reference BEM solution.

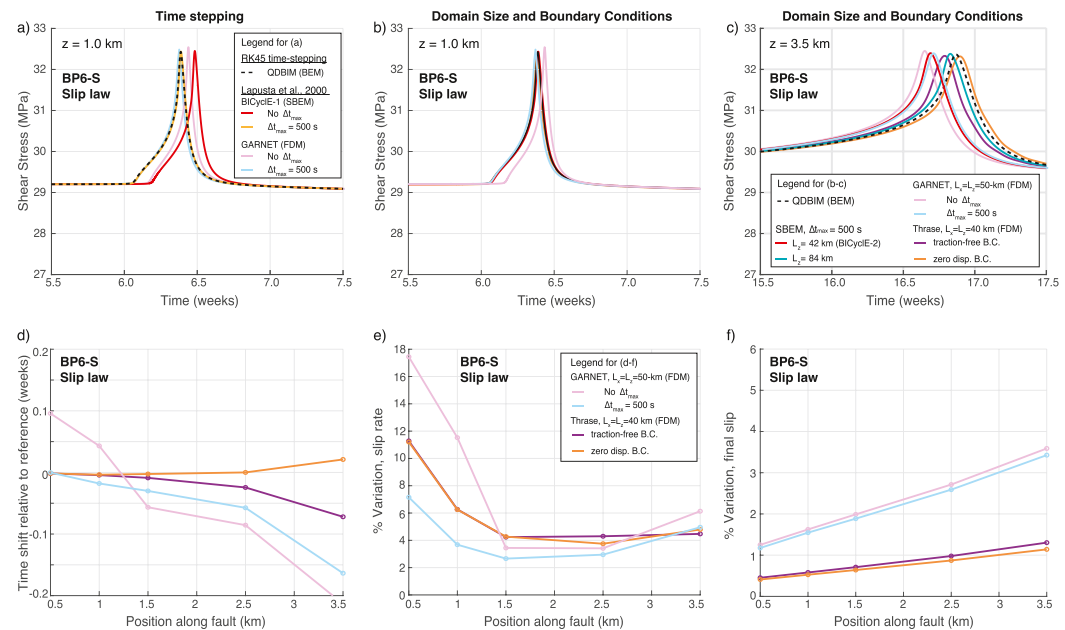


Figure 11. Comparison of simulation results using with different time-stepping and remote boundary conditions for FDM codes. (a) Similar to SBEM simulations (red), FDM simulations of BP6-QD-S using the time-stepping method of (Lapusta et al., 2000) (pink) show a lag in the slip front relative to the boundary element method, BEM solution using RK45 time stepping (dashed black). The discrepancy is reduced by implementing a maximum time step Δt_{\max} of 500 s in both FDM and SBEM simulations. (b)–(c) Sufficiently fine temporal sampling results in comparable solutions early on in the simulations of BP6-QD-S (b, $z = 1$ km), however the shear stress peak arrival time slightly differs for SBEM and FDM solutions with relatively small model domain sizes, and depends on the choice of traction-free or displacement remote boundary conditions (c, purple vs. orange). (d)–(f) Quantitative comparisons of (d) the time shift, and percent variation in local (e) slip rate and (f) final slip for the FDM simulations relative to the BEM reference solution.

domain size (Figures 10d and 10h). The results of these convergence tests with larger computational domains for the SBEM code BICycE-2 also explains differences between initial SBEM results for BICycE-1 and BICycE-2 that use domain sizes of $L_z = 52$ km and 42 km, respectively, versus the SBEM results of FastCycles which use a domain size of $L_z = 163.84$ km and shows greater agreement with other codes in Groups 1 and 3 (including the reference BEM solution, Figures 6–8).

The results of our convergence tests for the SBEM code BICycE suggest that the observed differences in the slip front arrival time and overall slip behavior in simulations of BP6-QD-A and BP6-QD-S for Group 4 codes (BICycE, GARNET, and FEBE) are largely due to choices in the computational domain size (L_x and/or $L_z \approx 40 - 50$ km). Note that these differences predominantly occur at points further from the injection site and closer to the domain boundaries. We find that the domain size-dependent effects also depend on the choice of remote boundary conditions applied for the relatively small domains. For example, BICycE and FEBE implement periodic boundary conditions along L_z , and FDM code GARNET implements traction-free remote boundary conditions. In contrast, the FDM code Thrase applies zero-displacement remote boundary conditions along a comparable model domain of ($L_x, L_z = 40$ km, 40 km) and achieves better agreement with results from other models using larger computational domain sizes (Figures 6, 7 and 11). Similar to our findings for the SBEM simulations, we find that increasing the temporal resolution for FDM simulations can improve the agreement in rupture arrival timing and slip behavior with the reference BEM solution at points closer to the injection site (Figure 11). The agreement at points further along in the aseismic rupture is more sensitive to the choice of traction-free versus zero-displacement remote boundary conditions and computational domain size, with better agreement to the reference BEM solution being achieved with zero-displacement boundary conditions (Figure 11).

Note that the choice of maximum time step of 500–1,000 s by some codes was motivated by stability requirements for explicit integration of the pore fluid pressure evolution when using adaptive time-stepping methods that do not directly consider the error in updating the pore pressure. The restriction on the time step for explicit integration methods of pore pressure diffusion is more stringent and depends on the spatial discretization. For example, the

BEM code QDBIM implements explicit pore pressure integration and uses RK45 adaptive time-stepping without an imposed maximum time step, but with error control on the pore pressure evolution. The maximum adaptive time step selected for simulations with a 10-m cell size is 1,307.5 s, and hence not much larger than the maximum time steps of 1,000 s imposed by some codes based on the diffusion time across the computational grid ($t_{\text{diff}} \propto \Delta z^2/\alpha = 1000$ s for $\Delta z = 10$ m). The maximum adaptive time step correspondingly increases or decreases by roughly a factor of 4 for a respective factor of two increase or decrease in the spatial discretization.

Implicit pore pressure integration methods should provide more stable solutions for larger time steps, though we find that the influence of the resolved pore pressure distribution on the frictional problem can be sensitive to the choice of time step. As an estimate of the maximum time step needed to determine an accurate solution of the pore pressure evolution, we consider the diffusion time across the process zone Λ , which reflects the minimum length scale that needs to be resolved for the frictional problem (e.g., Equation 10 in Section 3.3):

$$\Delta t_{\max} \leq \Lambda^2/\alpha \quad (14)$$

We find that the length of the process zone at points near the injection site $|z| < 1.5$ km is around 350 m for BP6-QD-A and 100 m for BP6-QD-S (Figures 12a and 12b), consistent with prior work demonstrating that the quasi-static process zone can be smaller for models using the slip law compared to the aging law (Ampuero & Rubin, 2008a). Given the hydraulic diffusivity of $0.1 \text{ m}^2/\text{s}$ used BP6-QD, this would suggest that the diffusion time Λ^2/α for points near the injection site is approximately 1.2×10^6 seconds for BP6-QD-A and 10^5 seconds for BP6-QD-S.

We compare the time series evolution of shear stress and slip rate at points near the injection site for results from the SBEM code BICycle-1 that implements implicit pore pressure integration using different imposed maximum time steps (Figures 12c–12f). As before, SBEM results using a larger maximum time step ($\Delta t_{\max} = 10^6$ s) show a lag in the slip front arrival relative to the reference BEM solution at points near the injection site. The discrepancy between the BEM and SBEM solutions decreases as the maximum time step is reduced. For a given maximum time step, the difference between the SBEM and reference BEM solution is larger for simulations of BP6-QD-S using the slip law compared to that of BP6-QD-A using aging laws. Considering the desire to resolve the pore fluid diffusion across the process zone by several time steps, we find that the this diffusion time is comparable to the maximum time steps used for the SBEM solutions to achieve good agreement with the reference BEM solution at points near the injection site, with Δt_{\max} less than $3 - 6 \times 10^5$ s for BP6-QD-A and less than 10^5 s for BP6-QD-S. This suggests that an estimate of the diffusion time Λ^2/α (e.g., using Equation 10 for the quasi-static cohesive zone estimate Λ_0 with the aging law) may serve as a reasonable guideline for estimating the maximum time step needed to determine an accurate solution of the pore pressure evolution for the one-way coupled frictional problem.

5. Summary and Discussion

We present code comparison results for two recent benchmark problems in the SEAS initiative considering 2-D models of fluid-induced aseismic slip governed by different treatments of fault friction using the aging (BP6-QD-A) and slip (BP6-QD-S) law formulations for frictional state evolution. We develop quantitative metrics to assist in exploring the sensitivity of simulated outcomes to computational domain size and temporal discretization, as well as to compute errors across model results against analytic and well-resolved reference solutions. Our community comparisons reveal excellent overall quantitative agreement in results for both benchmark problems across codes that implement different numerical methods, adaptive time-stepping approaches and integration strategies, with percent errors in simulated slip behavior mostly within within 5%. Errors in pore pressure and local slip evolution metrics are larger at fault locations near the fluid injection site ($|z| < 1.5$ km) where larger gradients in pore pressure change lead to more rapid variations in pore pressure, and correspondingly in slip, with percent errors in integrated slip rate up to 6% for models using the aging law and up to 18% for the slip law. The overall percent error in simulated aseismic slip after 2 years is generally within 3% at these near-injection site locations for results from both benchmark problems.

We find that further improvement in quantitative agreements for simulated slip behavior can be achieved by ensuring proper temporal resolution of both the pore pressure and slip evolution as well as consideration of model domain size and boundary conditions. While refining the temporal resolution improved the agreement in timing

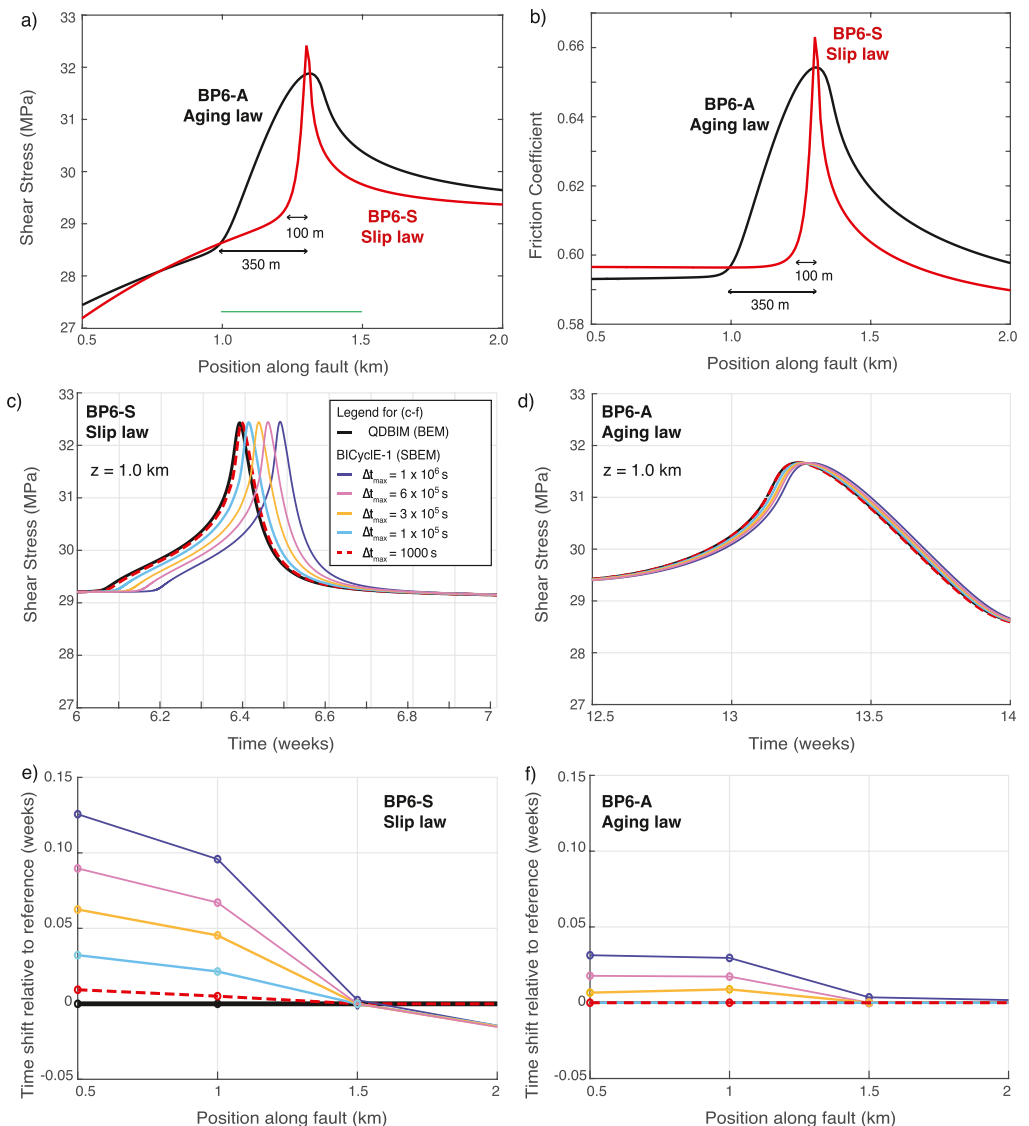


Figure 12. Comparison of simulation results using different maximum time steps Δt_{\max} for SBEM code BICyclE-1 with implicit pore pressure integration. (a)–(b) Spatial distribution of shear stress and friction coefficient for simulations using the aging (black) and slip (red) laws illustrating the breakdown of shear resistance at the front of the slip transient, often referred to as the process zone. The process zone is smaller (~ 100 m around $z = 1$ km) for the model using the slip law compared to the aging law (~ 350 m). (c)–(d) For points near the injection site, SBEM results using the time-stepping method of (Lapusta et al., 2000) with larger maximum time steps ($\Delta t_{\max} = 10^6$ s, dark blue) show a lag in the slip front arrival relative to the reference boundary element method, BEM solution (black). This discrepancy in arrival timing between the BEM and SBEM solutions decreases as the maximum time step is reduced. The difference is larger for models using the slip law (c) compared to the aging law (d) with the same maximum time step. (e)–(f) Quantitative comparison of the cross-correlation time shift for the SBEM slip rate time series relative to the reference BEM solution illustrating improved agreement in the temporal evolution of the slip rate at points near the injection site ($|z| < 1.5$ km) for simulations using smaller maximum time steps.

and slip rate evolution for points closer to the injection site in our comparisons, our convergence tests suggest that the effects of model domain size can have a larger influence on simulation results for BP6-QD, such as the total slip (Figure 10). These results reinforce our findings from prior benchmarks that choices in finite computational domain sizes and associated treatment of boundary conditions can influence aspects of model outcomes, with improved agreement for sufficiently large computational domains (Erickson et al., 2020, 2023; Jiang et al., 2022).

Increasing the temporal resolution and computational domain size of simulations can both lead to substantially higher computational cost. In particular, the implementation of a relatively small maximum time step in BP6-QD

can notably increase the number of required time steps for adaptive time-stepping methods. For example, results from the SBEM code BiCycle-2 utilizing a maximum time step of 500 s to resolve BP6-QD-S with explicit pore fluid pressure integration required 134,626 time steps for the 2-year simulation period. The BEM results of QDBIM for the same problem, including explicit pore pressure integration, but using RK45 adaptive time-stepping utilized 77,044 or almost half as many time steps. The reduction in required time steps for QDBIM without an imposed maximum time step is relatively modest given the error control on pore pressure and use of explicit integration. In comparison, the SBEM implementation of BiCycle-1 with implicit pore pressure integration using a more modest maximum time step of 10^5 s was able to achieve good agreement with the reference solution while only requiring around 11,000 time steps (Figure 12). Similarly, the number of time steps used by the FDM code GARNET with implicit pore pressure integration increased by a factor of 25 when implementing a maximum time step of 500 s compared to results using the adaptive method of (Lapusta et al., 2000), while resulting in relatively modest improved agreement with the reference solution (Figure 11).

The difference in computational expense further illustrates the value of adaptive time-stepping methods for simulating the potentially wide range of deformation rates throughout aseismic transients, here in the context of a single aseismic slip event, in addition to longer-term simulations of earthquake sequences. The trade-off between increased numerical accuracy and cost with increased temporal refinement depends on the specific numerical methodology and computational cost per time step, with the degree of acceptable error being dependent on the problem of interest. The quantitative agreements obtained across participating codes suggest that the problem formulations and numerical parameter choices (cell size, domain size, time-stepping) appear sufficient in order to obtain comparable results. The comparison metrics defined in this work, along with those in (Erickson et al., 2023; Jiang et al., 2022), represent continued efforts to develop and refine metrics that target different features of faulting and earthquake source processes and quantitatively assess SEAS model outcomes.

Our 2-D hydro-mechanical benchmark problems constitute important first steps toward verifying SEAS codes that simulate fault problems with multiple coupled physical processes. Comparisons of problems BP6-QD-A and BP6-QD-S using the aging and slip evolution laws, respectively, also illustrate how models of aseismic slip propagation can considerably vary in the timing, spatial extent, and amount of slip achieved with different treatments of fault friction evolution given the same time-dependent perturbation in pore fluid pressure. Depending on the application, the observed differences in simulated aseismic slip across our participating codes, including different choices in model domain size, may be considered relatively minor (within several percent error or millimeters of slip) over the 2-year period (Figure 7). However, given the nonlinear relationship between shear stress and slip in SEAS models and dynamic rupture, such small differences in slip and shear stress evolution could potentially influence aspects of earthquake nucleation or lead to different dynamic earthquake rupture behavior in more complicated fault models, including scenarios where such fluid-induced aseismic slip transient accelerates into dynamic rupture. Our future SEAS simulations will aim to consider such cases, including extensions with full inertial (wave-mediated) effects as well as additional physical ingredients, such as two-way coupling of hydro-mechanical processes, like mechanical dilatancy and compaction, thermo-hydro-mechanical processes such as the thermal pressurization of pore fluids, and their implications for earthquake nucleation and rupture propagation in physics-based models of seismic hazard.

Data Availability Statement

Our online platform (SCEC, 2024) hosts the simulation data for local and global fault properties and rupture times. The descriptions of benchmarks BP6 are available at (Lambert & Dunham, 2021) and included as Supporting Information S1. See the references in Table 1 for the availability of numerical codes.

References

- Abdelmeguid, M., Ma, X., & Elbanna, A. (2019). A novel hybrid finite element-spectral boundary integral scheme for modeling earthquake cycles: Application to rate and state faults with low-velocity zones. *Journal of Geophysical Research: Solid Earth*, 124(12), 12854–12881. <https://doi.org/10.1029/2019jb018036>
- Acosta, M., Passelègue, F. X., Schubnel, A., & Violay, M. (2018). Dynamic weakening during earthquakes controlled by fluid thermodynamics. *Nature Communications*, 9(1), 3074. <https://doi.org/10.1038/s41467-018-05603-9>
- Allègre, V., Brodsky, E. E., Xue, L., Nale, S. M., Parker, B. L., & Cherry, J. A. (2016). Using earth-tide induced water pressure changes to measure in situ permeability: A comparison with long-term pumping tests. *Water Resources Research*, 52(4), 3113–3126. <https://doi.org/10.1002/2015WR017346>

Acknowledgments

V.L. and E.M.D. designed the benchmark problem with input from B.A.E. and J.J. V.L., B.A.E., and J.J. organized the workshops for code verification exercises. V.L. analyzed the simulation results and led the writing of the manuscript. All remaining authors provided feedback on benchmark design, participated in the benchmark exercises (listed in Table 1), and/or helped with revising the manuscript. T.K. additionally helped with tests of model convergence and time-stepping; the other authors are listed alphabetically. V.L., B.A.E., and J.J. are supported by the Statewide California Earthquake Center (SCEC) awards 22079, 23144, and 24087. A SEAS-themed workshop was funded by SCEC award 22123. This research is SCEC Contribution No.13455. SCEC is funded by the National Science Foundation (NSF) Cooperative Agreement EAR-1600087 and the United States Geological Survey (USGS) Cooperative Agreement G17AC00047. V.L. was also supported by a National Science Foundation Postdoctoral Fellowship. S.O. was funded from an oversea research fellowship of Japan Society for the Promotion of Science. P.R. was supported by the European Research Council (ERC) Starting Grants 101040600 (HYQUAKE). M.L. and Y.v.D. are supported by the Dutch Research Council (NWO) grant DEEP.NL.2018.037. E.M.D. was supported by National Science Foundation award EAR-1947448. Y.Y. is supported by the Research Grants Council Postdoctoral Fellowship, University Grants Committee, Hong Kong (PDFS2223-4S08) and the Faculty of Science at the Chinese University of Hong Kong.

- Allison, K. L., & Dunham, E. M. (2018). Earthquake cycle simulations with rate-and-state friction and power-law viscoelasticity. *Tectonophysics*, 733, 232–256. <https://doi.org/10.1016/j.tecto.2017.10.021>
- Ampuero, J.-P., & Rubin, A. M. (2008a). Earthquake nucleation on rate and state faults: Aging and slip laws. *Journal of Geophysical Research*, 113(B1), B01302. <https://doi.org/10.1029/2007JB005082>
- Ampuero, J.-P., & Rubin, A. M. (2008b). Earthquake nucleation on rate and state faults – Aging and slip laws. *Journal of Geophysical Research: Solid Earth*, 113(B1), 1–21. <https://doi.org/10.1029/2007JB005082>
- Barall, M., & Harris, R. A. (2014). Metrics for comparing dynamic earthquake rupture simulations. *Seismological Research Letters*, 86(1), 223–235. <https://doi.org/10.1785/0220140122>
- Barbot, S. (2018). Asthenosphere flow modulated by megathrust earthquake cycles. *Geophysical Research Letters*, 45(12), 6018–6031. <https://doi.org/10.1029/2018GL078197>
- Barbot, S. (2022). A rate-state-and temperature-dependent friction law with competing healing mechanisms. *Journal of Geophysical Research: Solid Earth*, 127(11), e2022JB025106. <https://doi.org/10.1029/2022JB025106>
- Barbot, S., Lapusta, N., & Avouac, J.-P. (2012). Under the hood of the earthquake machine: Toward predictive modeling of the seismic cycle. *Science*, 336(6082), 707–710. <https://doi.org/10.1126/science.1218796>
- Beeler, N. M., Tullis, T. E., & Weeks, J. D. (1994). The roles of time and displacement in the evolution effect in rock friction. *Geophysical Research Letters*, 21(18), 1987–1990. <https://doi.org/10.1029/94GL01599>
- Ben-Zion, Y., & Rice, J. R. (1997). Dynamic simulations of slip on a smooth fault in an elastic solid. *Journal of Geophysical Research: Solid Earth*, 102(B8), 17771–17784. <https://doi.org/10.1029/97JB01341>
- Bhat, H. S., Olives, M., Dmowska, R., & Rice, J. R. (2007). Role of fault branches in earthquake rupture dynamics. *Journal of Geophysical Research*, 112(B11309), 16. <https://doi.org/10.1029/2007JB005027>
- Bhattacharya, P., Rubin, A. M., Bayart, E., Savage, H. M., & Marone, C. (2015). Critical evaluation of state evolution laws in rate and state friction: Fitting large velocity steps in simulated fault gouge with time-slip-and stress-dependent constitutive laws. *Journal of Geophysical Research: Solid Earth*, 120(9), 6365–6385. <https://doi.org/10.1002/2015JB012437>
- Bhattacharya, P., & Viesca, R. C. (2019). Fluid-induced aseismic fault slip outpaces pore-fluid migration. *Science*, 364(6439), 464–468. <https://doi.org/10.1126/science.aaw7354>
- Blanpied, M. L., Lockner, D. A., & Byerlee, J. D. (1991). Fault stability inferred from granite sliding experiments at hydrothermal conditions. *Geophysical Research Letters*, 18(4), 609–612. <https://doi.org/10.1029/91GL00469>
- Blanpied, M. L., Lockner, D. A., & Byerlee, J. D. (1995). Frictional slip of granite at hydrothermal conditions. *Journal of Geophysical Research*, 100(B7), 13045–13064. <https://doi.org/10.1029/95JB00862>
- Blanpied, M. L., Marone, C. J., Lockner, D. A., Byerlee, J. D., & King, D. P. (1998). Quantitative measure of the variation in fault rheology due to fluid-rock interactions. *Journal of Geophysical Research*, 103(B5), 9691–9712. <https://doi.org/10.1029/98JB00162>
- Burgmann, R. (2018). The geophysics, geology and mechanics of slow fault slip. *Earth and Planetary Science Letters*, 495, 112–134. <https://doi.org/10.1016/j.epsl.2018.04.062>
- Cappa, F., Guglielmi, Y., & De Barros, L. (2022). Transient evolution of permeability and friction in a slowly slipping fault activated by fluid pressurization. *Nature Communications*, 13(1), 3039. <https://doi.org/10.1038/s41467-022-30798-3>
- Cappa, F., Guglielmi, Y., Nussbaum, C., De Barros, L., & Birkholzer, J. (2022). Fluid migration in low-permeability faults driven by decoupling of fault slip and opening. *Nature Geoscience*, 15(9), 747–751. <https://doi.org/10.1038/s41561-022-00993-4>
- Cappa, F., Scuderi, M. M., Collettini, C., Guglielmi, Y., & Avouac, J.-P. (2019). Stabilization of fault slip by fluid injection in the laboratory and in situ. *Science Advances*, 5(3), eaau4065. Retrieved from <https://www.science.org/doi/abs/10.1126/sciadv.aau4065doi:10.1126/sciadv.aau4065>
- Carlsaw, H., & Jaeger, J. (1959). *Conduction of heat in solids*. Clarendon Press. Retrieved from <https://books.google.com/books?id=y20sAAAYAAJ>
- Cattania, C. (2019). Complex earthquake behavior on simple faults. *submitted to Geophysical Research Letters*. <https://doi.org/10.31223/osf.io/hgbjx>
- Chen, T., & Lapusta, N. (2009). Scaling of small repeating earthquakes explained by interaction of seismic and aseismic slip in a rate and state fault model. *Journal of Geophysical Research*, 114(B01311), B01311. <https://doi.org/10.1029/2008JB005749>
- Cochard, A., & Rice, J. R. (1997). A spectral method for numerical elastodynamic fracture analysis without spatial replication of the rupture event. *Journal of the Mechanics and Physics of Solids*, 45(8), 1393–1418. [https://doi.org/10.1016/S0022-5096\(97\)00004-5](https://doi.org/10.1016/S0022-5096(97)00004-5)
- Day, S. M. (1982). Three-dimensional finite difference simulation of fault dynamics: Rectangular faults with fixed rupture velocity. *Bulletin of the Seismological Society of America*, 72(3), 705–727.
- Day, S. M., Dalguer, L. A., Lapusta, N., & Liu, Y. (2005). Comparison of finite difference and boundary integral solutions to three-dimensional spontaneous rupture. *Journal of Geophysical Research: Solid Earth*, 110(B12), B12307. <https://doi.org/10.1029/2005JB003813>
- Dieterich, J. H. (1979). Modeling of rock friction 1. Experimental results and constitutive equations. *Journal of Geophysical Research*, 84(B5), 2161–2168. <https://doi.org/10.1029/jb084ib05p02161>
- Dieterich, J. H. (1992). Earthquake nucleation on faults with rate- and state-dependent strength. *Tectonophysics*, 211(1–4), 115–134. [https://doi.org/10.1016/0040-1951\(92\)90055-b](https://doi.org/10.1016/0040-1951(92)90055-b)
- Dieterich, J. H. (2007). Applications of rate- and state-dependent friction to models of fault slip and earthquake occurrence. In G. Schubert (Ed.), *Treatise on geophysics* (pp. 107–129). Elsevier. <https://doi.org/10.1016/B978-044452748-6.00065-1>
- Dublanchet, P. (2019). Fluid driven shear cracks on a strengthening rate-and-state frictional fault. *Journal of the Mechanics and Physics of Solids*, 132, 103672. <https://doi.org/10.1016/j.jmps.2019.07.015>
- Dunham, E. M., Belanger, D., Cong, L., & Kozdon, J. E. (2011a). Earthquake ruptures with strongly rate-weakening friction and off-fault plasticity, Part 1: Planar faults. *Bulletin of the Seismological Society of America*, 101(5), 2296–2307. <https://doi.org/10.1785/0120100075>
- Dunham, E. M., Belanger, D., Cong, L., & Kozdon, J. E. (2011b). Earthquake ruptures with strongly rate-weakening friction and off-fault plasticity, Part 2: Nonplanar faults. *Bulletin of the Seismological Society of America*, 101(5), 2308–2322. <https://doi.org/10.1785/0120100076>
- Ellsworth, W. L. (2013). Injection-induced earthquakes. *Science*, 341(6142), 1225942. <https://doi.org/10.1126/science.1225942>
- Erickson, B. A., & Dunham, E. M. (2014). An efficient numerical method for earthquake cycles in heterogeneous media: Alternating subbasin and surface-rupturing events on faults crossing a sedimentary basin. *Journal of Geophysical Research: Solid Earth*, 119(4), 3290–3316. <https://doi.org/10.1002/2013JB010614>
- Erickson, B. A., Jiang, J., Barall, M., Lapusta, N., Dunham, E. M., Harris, R., et al. (2020). The community code verification exercise for simulating sequences of earthquakes and aseismic slip (SEAS). *Seismological Research Letters*, 91(2A), 874–890. <https://doi.org/10.1785/0220190248>

- Erickson, B. A., Jiang, J., Lambert, V., Barbot, S. D., Abdelmeguid, M., Almquist, M., et al. (2023). Incorporating full elastodynamic effects and dipping fault geometries in community code verification exercises for simulations of earthquake sequences and aseismic slip (SEAS). *Bulletin of the Seismological Society of America*, 113(2), 499–523. <https://doi.org/10.1785/0120220066>
- Erickson, B. A., Kozdon, J. E., & Harvey, T. (2022). A non-stiff summation-by-parts finite difference method for the scalar wave equation in second order form: Characteristic boundary conditions and nonlinear interfaces. *Journal of Scientific Computing*, 93(1), 17. <https://doi.org/10.1007/s10915-022-01961-1>
- Eyre, T. S., Eaton, D. W., Garagash, D. I., Zecevic, M., Venieri, M., Weir, R., & Lawton, D. C. (2019). The role of aseismic slip in hydraulic fracturing-induced seismicity. *Science Advances*, 5(8), eaav7172. <https://doi.org/10.1126/sciadv.aav7172>
- Frank, W., Shapiro, N., Husker, A., Kostoglodov, V., Bhat, H., & Campillo, M. (2015). Along-fault pore-pressure evolution during a slow-slip event in guerero, Mexico. *Earth and Planetary Science Letters*, 413, 135–143. <https://doi.org/10.1016/j.epsl.2014.12.051>
- Freund, L. (1998). *Dynamic fracture mechanics*. Cambridge University Press. Retrieved from <https://books.google.com/books?id=Cij0jwEACAAJ>
- Gabriel, A.-A., Ampuero, J.-P., Dalguer, L. A., & Mai, P. M. (2012). The transition of dynamic rupture styles in elastic media under velocity-weakening friction. *Journal of Geophysical Research*, 117(B9), B09311. <https://doi.org/10.1029/2012JB009468>
- Garagash, D. I. (2021). Fracture mechanics of rate-and-state faults and fluid injection induced slip. *Philosophical Transactions of the Royal Society A: Mathematical, Physical and Engineering Sciences*, 379(2196), 20200129. <https://doi.org/10.1098/rsta.2020.0129>
- Guglielmi, Y., Cappa, F., Avouac, J.-P., Henry, P., & Elsworth, D. (2015). Seismicity triggered by fluid injection-induced aseismic slip. *Science*, 348(6240), 1224–1226. <https://doi.org/10.1126/science.aab0476>
- Guglielmi, Y., Nussbaum, C., Cappa, F., De Barros, L., Rutqvist, J., & Birkholzer, J. (2021). Field-scale fault reactivation experiments by fluid injection highlight aseismic leakage in caprock analogs: Implications for co2 sequestration. *International Journal of Greenhouse Gas Control*, 111, 103471. <https://doi.org/10.1016/j.ijgpc.2021.103471>
- Hajarolasladi, S., & Elbanna, A. E. (2017). A new hybrid numerical scheme for modelling elastodynamics in unbounded media with near-source heterogeneities. *Geophysical Journal International*, 211(2), 851–864. <https://doi.org/10.1093/gji/ggx337>
- Harris, R. A., Barall, M., Aagaard, B., Ma, S., Roten, D., Olsen, K., et al. (2018). A suite of exercises for verifying dynamic earthquake rupture codes. *Seismological Research Letters*, 89(3), 1146–1162. <https://doi.org/10.1785/0220170222>
- Harris, R. A., Barall, M., Archuleta, R., Dunham, E. M., Aagaard, B., Ampuero, J. P., et al. (2009). The SCEC/USGS dynamic earthquake rupture code verification exercise. *Seismological Research Letters*, 80(1), 119–126. <https://doi.org/10.1785/gssrl.80.1.119>
- Hauksson, E., Andrews, J., Plesch, A., Shaw, J. H., & Shelly, D. R. (2016). The 2015 fillmore earthquake swarm and possible crustal deformation mechanisms near the bottom of the eastern ventura basin, California. *Seismological Research Letters*, 87(4), 807–815. <https://doi.org/10.1785/0220160020>
- Hubbard, J., & Mallick, R. (2021). An overlooked hazard can cause damage weeks after an earthquake strikes. *Temblor*. <https://doi.org/10.32858/temblor.212>
- Ito, Y., Hino, R., Kido, M., Fujimoto, H., Osada, Y., Inazu, D., et al. (2013). Episodic slow slip events in the Japan subduction zone before the 2011 Tohoku-Oki earthquake. *Tectonophysics*, 600, 14–26. <https://doi.org/10.1016/j.tecto.2012.08.022>
- Jacquey, A. B., & Viesca, R. C. (2023). Nucleation and arrest of fluid-induced aseismic slip. *Geophysical Research Letters*, 50(4), e2022GL101228. <https://doi.org/10.1029/2022GL101228>
- Jiang, J., Erickson, B. A., Lambert, V. R., Ampuero, J.-P., Ando, R., Barbot, S. D., et al. (2022). Community-driven code comparisons for three-dimensional dynamic modeling of sequences of earthquakes and aseismic slip. *Journal of Geophysical Research: Solid Earth*, 127(3), e2021JB023519. <https://doi.org/10.1029/2021JB023519>
- Jiang, J., & Lapusta, N. (2016). Deeper penetration of large earthquakes on seismically quiescent faults. *Science*, 352(6291), 1293–1297. <https://doi.org/10.1126/science.aaf1496>
- Kaneko, Y., Avouac, J.-P., & Lapusta, N. (2010). Towards inferring earthquake patterns from geodetic observations of interseismic coupling. *Nature Geoscience*, 3(5), 363–369. <https://doi.org/10.1038/ngeo843>
- Kato, A., Obara, K., Igarashi, T., Tsuruoka, H., Nakagawa, S., & Hirata, N. (2012). Propagation of slow slip leading up to the 2011 Mw 9.0 Tohoku-Oki earthquake. *Science*, 335(6069), 705–708. <https://doi.org/10.1126/science.1215141>
- Kato, N. (2023). Numerical simulation of episodic aseismic slip events as incomplete nucleation of seismic slip due to heterogeneous stress distribution. *Bulletin of the Seismological Society of America*, 113(5), 2009–2025. <https://doi.org/10.1785/0120230048>
- Khoshmanesh, M., & Shirzaei, M. (2018). Episodic creep events on the san andreas fault caused by pore pressure variations. *Nature Geoscience*, 11(8), 610–614. <https://doi.org/10.1038/s41561-018-0160-2>
- Kozdon, J., Erickson, B. A., & Wilcox, L. C. (2020). Hybridized summation-by-parts finite difference methods. *Journal of Scientific Computing*, 87(85), 1–28. <https://doi.org/10.1007/s10915-021-01448-5>
- Kozdon, J. E., & Dunham, E. M. (2013). Rupture to the trench: Dynamic rupture simulations of the 11 March 2011 Tohoku earthquake. *Bulletin of the Seismological Society of America*, 103(2B), 1275–1289. <https://doi.org/10.1785/0120120136>
- Lambert, V., & Barbot, S. (2016). Contribution of viscoelastic flow in earthquake cycles within the lithosphere-asthenosphere system. *Geophysical Research Letters*, 43(19), 10142–10154. <https://doi.org/10.1002/2016GL070345>
- Lambert, V., & Dunham, E. M. (2021). Seas Benchmark Problems BP6-QD-A/S/C. Retrieved from https://strike.scec.org/cvws/seas/download/SEAS_BP6_Nov18.pdf
- Lambert, V., Lapusta, N., & Faulkner, D. (2021). Scale dependence of earthquake rupture prestress in models with enhanced weakening: Implications for event statistics and inferences of fault stress. *Journal of Geophysical Research: Solid Earth*, 126(10), e2021JB021886. <https://doi.org/10.1029/2021JB021886>
- Lambert, V., Lapusta, N., & Perry, S. (2021). Propagation of large earthquakes as self-healing pulses or mild cracks. *Nature*, 591(7849), 252–258. <https://doi.org/10.1038/s41586-021-03248-1>
- Lapusta, N., & Liu, Y. (2009). Three-dimensional boundary integral modeling of spontaneous earthquake sequences and aseismic slip. *Journal of Geophysical Research: Solid Earth*, 114(B9), 1–25. <https://doi.org/10.1029/2008JB005934>
- Lapusta, N., & Rice, J. R. (2003). Nucleation and early seismic propagation of small and large events in a crustal earthquake model. *Journal of Geophysical Research*, 108(B4), 2205. <https://doi.org/10.1029/2001jb000793>
- Lapusta, N., Rice, J. R., Ben-Zion, Y., & Zheng, G. (2000). Elastodynamic analysis for slow tectonic loading with spontaneous rupture episodes on faults with rate- and state-dependent friction. *Journal of Geophysical Research*, 105, 765–789. <https://doi.org/10.1029/2000JB900250>
- Laroche, S., Lapusta, N., Ampuero, J.-P., & Cappa, F. (2021). Constraining fault friction and stability with fluid-injection field experiments. *Geophysical Research Letters*, 48(10), e2020GL091188. <https://doi.org/10.1029/2020GL091188>
- Lee, K.-K., Ellsworth, W. L., Giardini, D., Townend, J., Ge, S., Shimamoto, T., et al. (2019). Managing injection-induced seismic risks. *Science*, 364(6442), 730–732. <https://doi.org/10.1126/science.aax1878>

- Li, M., Pranger, C., & van Dinther, Y. (2022). Characteristics of earthquake cycles: A cross-dimensional comparison of 0D to 3D numerical models. *Journal of Geophysical Research: Solid Earth*, 127(8), e2021JB023726. <https://doi.org/10.1029/2021JB023726>
- Liu, Y. (2014). Source scaling relations and along-strike segmentation of slow slip events in a 3-D subduction fault model. *Journal of Geophysical Research: Solid Earth*, 119(8), 6512–6533. <https://doi.org/10.1002/2014JB011144>
- Liu, Y., & Rice, J. R. (2005). Aseismic slip transients emerge spontaneously in three-dimensional rate and state modeling of subduction earthquake sequences. *Journal of Geophysical Research*, 110(B8), B08307. <https://doi.org/10.1029/2004JB003424>
- Liu, Y., & Rice, J. R. (2007). Spontaneous and triggered aseismic deformation transients in a subduction fault model. *Journal of Geophysical Research*, 112(B9), B09404. <https://doi.org/10.1029/2007JB004930>
- Llanos, E. M., Zarrouk, S. J., & Hogarth, R. A. (2015). Numerical model of the habanero geothermal reservoir, Australia. *Geothermics*, 53, 308–319. <https://doi.org/10.1016/j.geothermics.2014.07.008>
- Lozos, J. C., Oglesby, D. D., Duan, B., & Wesnousky, S. G. (2011). The effects of double fault bends on rupture propagation: A geometrical parameter study. *Bulletin of the Seismological Society of America*, 101(1), 385–398. <https://doi.org/10.1785/0120100029>
- Luo, H., & Wang, K. (2022). Finding simplicity in the complexity of postseismic coastal uplift and subsidence following great subduction earthquakes. *Journal of Geophysical Research: Solid Earth*, 127(10), e2022JB024471. <https://doi.org/10.1029/2022JB024471>
- Ma, X., & Elbanna, A. (2019). Dynamic rupture propagation on fault planes with explicit representation of short branches. *Earth and Planetary Science Letters*, 523, 115702. <https://doi.org/10.1016/j.epsl.2019.07.005>
- Marone, C. (1998). Laboratory-derived friction laws and their application to seismic faulting. *Annual Review of Earth and Planetary Sciences*, 26(1), 643–696. <https://doi.org/10.1146/annurev.earth.26.1.643>
- McGarr, A., Bekins, B., Burkhardt, N., Dewey, J., Earle, P., Ellsworth, W., et al. (2015). Coping with earthquakes induced by fluid injection. *Science*, 347(6224), 830–831. <https://doi.org/10.1126/science.aaa0494>
- Mia, M. S., Abdelmeguid, M., & Elbanna, A. E. (2022). Spatio-temporal clustering of seismicity enabled by off-fault plasticity. *Geophysical Research Letters*, 49(8), e2021GL097601. <https://doi.org/10.1029/2021GL097601>
- Michel, S., Gualandi, A., & Avouac, J.-P. (2019). Interseismic coupling and slow slip events on the Cascadia megathrust. *Pure and Applied Geophysics*, 176(9), 3867–3891. <https://doi.org/10.1007/s00024-018-1991-x>
- Muto, J., Moore, J. D. P., Barbot, S., Iiuma, T., Ohta, Y., & Iwamori, H. (2019). Coupled afterslip and transient mantle flow after the 2011 Tohoku earthquake. *Science Advances*, 5(9), eaaw1164. <https://doi.org/10.1126/sciadv.aaw1164>
- Nielsen, S. B., Carlson, J., & Olsen, K. B. (2000). Influence of friction and fault geometry on earthquake rupture. *Journal of Geophysical Research*, 105(B3), 6069–6088. <https://doi.org/10.1029/1999jb900350>
- Noda, H., Dunham, E. M., & Rice, J. R. (2009). Earthquake ruptures with thermal weakening and the operation of major faults at low overall stress levels. *Journal of Geophysical Research*, 114(B7), B07302. <https://doi.org/10.1029/2008JB006143>
- Noda, H., & Lapusta, N. (2013). Stable creeping fault segments can become destructive as a result of dynamic weakening. *Nature*, 493(7433), 518–521. <https://doi.org/10.1038/nature11703>
- Noda, H., Lapusta, N., & Kanamori, H. (2013). Comparison of average stress drop measures for ruptures with heterogeneous stress change and implications for earthquake physics. *Geophysical Journal International*, 193(3), 1691–1712. <https://doi.org/10.1093/gji/gjt074>
- Noël, C., Giorgetti, C., Scuderi, M. M., Collettini, C., & Marone, C. (2023). The effect of shear displacement and wear on fault stability: Laboratory constraints. *Journal of Geophysical Research: Solid Earth*, 128(4), e2022JB026191. <https://doi.org/10.1029/2022JB026191>
- Olsen, K. B., Madariaga, R., & Archuleta, R. J. (1997). Three-dimensional dynamic simulation of the 1992 Landers earthquake. *Science*, 278(5339), 834–838. <https://doi.org/10.1126/science.278.5339.834>
- Ozawa, S., Murakami, M., Kaidzu, M., Tada, T., Sagiya, T., Hatanaka, Y., et al. (2002). Detection and monitoring of ongoing aseismic slip in the Tokai region, central Japan. *Science*, 298(5595), 1009–1012. <https://doi.org/10.1126/science.1076780>
- Ozawa, S., Yang, Y., & Dunham, E. M. (2024). Fault-Valve instability: A mechanism for slow slip events. <https://doi.org/10.22541/essoar.171291623.31088922/v1>
- Ozawa, S. W., Hatano, T., & Kame, N. (2019). Longer migration and spontaneous decay of aseismic slip pulse caused by fault roughness. *Geophysical Research Letters*, 46(2), 636–643. <https://doi.org/10.1029/2018GL081465>
- Palmer, A. C., & Rice, J. R. (1973). The growth of slip surfaces in the progressive failure of over-consolidated clay. *Proceedings of the Royal Society A: Mathematical, Physical and Engineering Sciences*, 332(1591), 527–548. <https://doi.org/10.1098/rspa.1973.0040>
- Perfettini, H., & Ampuero, J.-P. (2008). Dynamics of a velocity strengthening fault region: Implications for slow earthquakes and postseismic slip. *Journal of Geophysical Research: Solid Earth*, 113(B9), 1–22. <https://doi.org/10.1029/2007JB005398>
- Pignalberi, F., Giorgetti, C., Noël, C., Marone, C., Collettini, C., & Scuderi, M. M. (2024). The effect of normal stress oscillations on fault slip behavior near the stability transition from stable to unstable motion. *Journal of Geophysical Research: Solid Earth*, 129(2), e2023JB027470. <https://doi.org/10.1029/2023JB027470>
- Pranger, C. (2020). *Unstable physical processes operating on self-governing fault systems, improved modeling methodology (Unpublished doctoral dissertation)*. ETH Zurich.
- Rice, J. R., & Ruina, A. L. (1983). Stability of steady frictional slipping. *Journal of Applied Mechanics*, 50(2), 343–349. <https://doi.org/10.1115/1.3167042>
- Richards-Dinger, K., & Dieterich, J. H. (2012). RSQSim earthquake simulator. *Seismological Research Letters*, 83(6), 983–990. <https://doi.org/10.1785/0220120105>
- Ripperger, J., Ampuero, J.-P., Mai, P. M., & Giardini, D. (2007). Earthquake source characteristics from dynamic rupture with constrained stochastic fault stress. *Journal of Geophysical Research: Solid Earth*, 112(B4). <https://doi.org/10.1029/2006JB004515>
- Rogers, G., & Dragert, H. (2003). Episodic tremor and slip on the Cascadia subduction zone: The chatter of silent slip. *Science*, 300(5627), 1942–1943. <https://doi.org/10.1126/science.1084783>
- Romanet, P., Bhat, H. S., Jolivet, R., & Madariaga, R. (2018). Fast and slow slip events emerge due to fault geometrical complexity. *Geophysical Research Letters*, 45(10), 4809–4819. <https://doi.org/10.1029/2018GL077579>
- Romanet, P., & Ozawa, S. (2021). Fully dynamic earthquake cycle simulations on a nonplanar fault using the spectral boundary integral element method (sBIEM). *Bulletin of the Seismological Society of America*, 112(1), 78–97. <https://doi.org/10.1785/0120210178>
- Ross, Z. E., Trugman, D. T., Azizzadenesheli, K., & Anandkumar, A. (2020). Directivity modes of earthquake populations with unsupervised learning. *Journal of Geophysical Research: Solid Earth*, 125(2), e2019JB018299. <https://doi.org/10.1029/2019JB018299>
- Ruina, A. (1983). Slip instability and state variable friction laws. *Journal of Geophysical Research*, 88(B12), 10359–10370. <https://doi.org/10.1029/jb088ib12p10359>
- Ruiz, S., Metois, M., Fuenzalida, A., Ruiz, J., Leyton, F., Grandin, R., et al. (2014). Intense foreshocks and a slow slip event preceded the 2014 Iquique Mw 8.1 earthquake. *Science*, 345(6201), 1165–1169. <https://doi.org/10.1126/science.1256074>

- Saez, A., Lecampion, B., Bhattacharya, P., & Viesca, R. C. (2022). Three-dimensional fluid-driven stable frictional ruptures. *Journal of the Mechanics and Physics of Solids*, 160, 104754. <https://doi.org/10.1016/j.jmps.2021.104754>
- SCEC, S. (2024). The SCEC sequences of earthquakes and aseismic slip Project [Dataset]. *The SCEC Sequences of Earthquakes and Aseismic Slip Project*. <https://strike.scec.org/cvws/cgi-bin/seas.cgi.SCEC>
- Schwartz, S. Y., & Rokosky, J. M. (2007). Slow slip events and seismic tremor at circum-pacific subduction zones. *Reviews of Geophysics*, 45(3), RG3004. <https://doi.org/10.1029/2006rg000208>
- Segall, P., & Bradley, A. M. (2012). Slow-slip evolves into megathrust earthquakes in 2d numerical simulations. *Geophysical Research Letters*, 39(18), L18308. <https://doi.org/10.1029/2012GL052811>
- Segall, P., & Rice, J. R. (1995). Dilatancy, compaction, and slip instability of a fluid-infiltrated fault. *Journal of Geophysical Research*, 100(B11), 22155–22171. <https://doi.org/10.1029/95JB02403>
- Segall, P., & Rice, J. R. (2006). Does shear heating of pore fluid contribute to earthquake nucleation? *Journal of Geophysical Research*, 111(B09316), 17. <https://doi.org/10.1029/2005jb004129>
- Segall, P., Rubin, A. M., Bradley, A. M., & Rice, J. R. (2010). Dilatant strengthening as a mechanism for slow slip events. *Journal of Geophysical Research*, 115(B12), B12305. <https://doi.org/10.1029/2010JB007449>
- Shaw, B. E., Milner, K. R., Field, E. H., Richards-Dinger, K., Gilchrist, J. J., Dieterich, J. H., & Jordan, T. H. (2018). A physics-based earthquake simulator replicates seismic hazard statistics across California. *Science Advances*, 4(8). <https://doi.org/10.1126/sciadv.aau0688>
- Shelly, D. R., Beroza, G. C., & Ide, S. (2007). Complex evolution of transient slip derived from precise tremor locations in western shikoku, Japan. *Geochemistry, Geophysics, Geosystems*, 8(10), Q10014. <https://doi.org/10.1029/2007GC001640>
- Shi, Z., & Day, S. M. (2013). Rupture dynamics and ground motion from 3-d rough-fault simulations. *Journal of Geophysical Research: Solid Earth*, 118(3), 1122–1141. <https://doi.org/10.1002/jgrb.50094>
- Shimamoto, T., & Noda, H. (2014). A friction to flow constitutive law and its application to a 2-d modeling of earthquakes. *Journal of Geophysical Research: Solid Earth*, 119(11), 8089–8106. <https://doi.org/10.1002/2014JB011170>
- Thakur, P., Huang, Y., & Kaneko, Y. (2020). Effects of low-velocity fault damage zones on long-term earthquake behaviors on mature strike-slip faults. *Journal of Geophysical Research: Solid Earth*, 125(8), e2020JB019587. <https://doi.org/10.1029/2020JB019587>
- Tullis, T. E., Richards-Dinger, K., Barall, M., Dieterich, J. H., Field, E. H., Heien, E. M., et al. (2012). Generic earthquake simulator. *Seismological Research Letters*, 83(6), 959–963. <https://doi.org/10.1785/0220120093>
- Ulrich, T., Gabriel, A.-A., Ampuero, J.-P., & Xu, W. (2019). Dynamic viability of the 2016 Mw 7.8 Kaikoura earthquake cascade on weak crustal faults. *Nature Communications*, 10(1), 1213. <https://doi.org/10.1038/s41467-019-109125-w>
- Uphoff, C., May, D. A., & Gabriel, A.-A. (2022). A discontinuous Galerkin method for sequences of earthquakes and aseismic slip on multiple faults using unstructured curvilinear grids. *Geophysical Journal International*, 233(1), 586–626. <https://doi.org/10.1093/gji/gjac467>
- Viesca, R. C. (2021). Self-similar fault slip in response to fluid injection. *Journal of Fluid Mechanics*, 928, A29. <https://doi.org/10.1017/jfm.2021.825>
- Wei, S., Avouac, J.-P., Hudnut, K. W., Donnellan, A., Parker, J. W., Graves, R. W., et al. (2015). The 2012 brawley swarm triggered by injection-induced aseismic slip. *Earth and Planetary Science Letters*, 422, 115–125. <https://doi.org/10.1016/j.epsl.2015.03.054>
- Xu, J., Zhang, H., & Chen, X. (2015). Rupture phase diagrams for a planar fault in 3-d full-space and half-space. *Geophysical Journal International*, 202(3), 2194–2206. <https://doi.org/10.1093/gji/ggv284>
- Xue, L., Brodsky, E. E., Erskine, J., Fulton, P. M., & Carter, R. (2016). A permeability and compliance contrast measured hydrogeologically on the san andreas fault. *Geochemistry, Geophysics, Geosystems*, 17(3), 858–871. <https://doi.org/10.1002/2015GC006167>
- Yang, Y., & Dunham, E. M. (2021). Effect of porosity and permeability evolution on injection-induced aseismic slip. *Journal of Geophysical Research: Solid Earth*, 126(7), e2020JB021258. <https://doi.org/10.1029/2020JB021258>
- Yang, Y., & Dunham, E. M. (2023). Influence of creep compaction and dilatancy on earthquake sequences and slow slip. *Journal of Geophysical Research: Solid Earth*, 128(4), e2022JB025969. <https://doi.org/10.1029/2022JB025969>
- Zhu, W., Allison, K. L., Dunham, E. M., & Yang, Y. (2020). Fault valving and pore pressure evolution in simulations of earthquake sequences and aseismic slip. *Nature Communications*, 11(1), 4833. <https://doi.org/10.1038/s41467-020-18598-z>